Coherent Manipulation of Multi-Partite Quantum States in a Qubit-TLS System via Landau-Zener Transition

by

Bo Mao

Submitted to the graduate degree program in Physics
and the Graduate Faculty of the University of Kansas
in partial fulfillment of the requirements for the degree of
Doctor of Philosophy.

Chairperson Siyuan Han

Committee members

Danny Marfatia

Judy Wu

Hui Zhao

Rongqing Hui

Date defended: July 15, 2010

The Dissertation Committee for Bo Mao certifies

that this is the approved version of the following dissertation:

Coherent Manipulation of Multi-Partite Quantum States in a Qubit-TLS System via Landau-Zener Transition

Committee:

_____

Chairperson Siyuan Han

_____

Danny Marfatia

_____

Judy Wu

_____

Hui Zhao

_____

Rongqing Hui

Date approved: _____

Abstract

A radio frequency (rf) superconducting quantum interference device (SQUID) is a macroscopic quantum object consisting of a superconducting loop interrupted by a Josephson junction. Superconducting phase quantum bits (qubits) based on rf SQUIDs have been proven to be one of the most promising candidates for building a quantum computer. They exploit the unique resources of quantum superposition and entanglement and are exponentially faster than classical computers in solving certain problems, such as factoring. Compared to other approaches to quantum computing, superconducting phase qubits allow stronger and more flexible inter-qubit coupling and thus are easier to scale up. However, phase qubits couple to the environment and are subject to considerable decoherence. The resulting coherence time (also called decoherence time) is on the order of 10^2 ns, about two orders of magnitude shorter than that required for fault-tolerant quantum computing. One possible solution is to develop faster quantum gates in phase qubits.

In this dissertation, coherent manipulation of multi-partite quantum states via Landau-Zener (LZ) transitions was investigated in a phase qubit, which was coupled to two microscopic two-level systems (TLSs) embedded in the tunnel barrier of the Josephson junction. The qubit chip was measured at temperatures below 30 mK in an ultra-low noise environment with excellent electrical and magnetic filtering and shielding. All parameters of the phase qubit were calibrated independently. The phase qubit's decoherence times have been carefully measured as well. Fast and precise

coherent control of the tripartite quantum states has been successfully demonstrated by the observation of the Landau-Zener-Stückelberg (LZS) interference in the coupled qubit-TLS system. Furthermore, it is shown that utilizing LZ transitions to create multi-partite entangled states, such as the W state, is significantly more efficient than conventional methods which require a sequence of single-qubit and two-qubit gates. Hence, coherent manipulation of multi-partite quantum states via LZ transitions is a promising basis for a new family of fast multi-qubit quantum gates.

Table of Contents

List of Symbols

Symbol	Description
AQC	adiabatic quantum computing
C	junction capacitance
CJJ	compound Josephson junction
CPF	copper power filter
e	elementary charge
E_J	maximum Josephson energy
f_0	transition frequency ($= \Delta E_{10} / h$)
$G(x;\sigma)$	Gaussian function of x with width σ
H	Hamiltonian
I_b	bias current
I_c	critical current of junction
I_p	circulating/persistent current in SQUID loop
I_{rf}	microwave-induced current
JJ	Josephson junction
k_B	Boltzmann's constant
L	rf SQUID loop inductance
L_{dc}	dc SQUID loop inductance
LZ	Landau-Zener
LZS	Landau-Zener-Stückelberg
MQC	macroscopic quantum coherence

MRT	macroscopic resonant tunneling
MQT	macroscopic quantum tunneling
M_{sq}	mutual inductance between qubit and dc SQUID
P_1	excitation probability
P_{LZ}	Landau-Zener transition probability
P_t	tunneling probability
QC	quantum computing
QED	quantum electrodynamics
qubit	quantum bit
rms	root mean square
RWA	rotating wave approximation
$R_{\vec{n}}(\theta)$	operator of rotation about vector $\vec{n}$ by an angle θ
SQUID	superconducting quantum interference device
T	temperature
T_1	energy relaxation time
T_2	decoherence time
T_{2E}	decoherence time from spin echo signal
$1/T_\varphi$	pure dephasing rate from Ramsey fringe signal
$1/T_{\varphi E}$	pure dephasing rate from spin echo signal
TLS	two-level system
U	potential energy
v	sweeping rate of energy

β_L	parameter of rf SQUID ($= 2\pi L I_c / \Phi_0$)
β_{L0}	maximum β_L of CJJ rf SQUID
φ	phase, phase difference
Φ	total magnetic flux in SQUID loop
Φ_0	magnetic flux quantum (2.07×10^{-15} Wb)
Φ_b	position of bottom of well
Φ_{mod}	external flux bias of dc SQUID
Φ_x	external flux bias of rf SQUID
Φ_{xdc}	external flux bias of CJJ rf SQUID
Δ	tunnel splitting
$\Delta\Phi_{\mathrm{m}}$	distance between the two potential minima at $\Phi_x = \Phi_0 / 2$
$\Delta\Phi_{x\_MRT}$	spacing in flux bias between adjacent MRT peaks around $\Phi_x = \Phi_0 / 2$
$\Delta E_{10}, \hbar\omega_{10}$	energy level spacing between qubit states
$\hbar$, h	reduced Planck's constant, Planck's constant
Ω	angular frequency of Rabi oscillation
Δf, $\Delta\omega / 2\pi$	frequency detuning
ω_p	small oscillation frequency around bottom of well
ρ	density matrix
σ	Gaussian line width

List of Figures

Acknowledgements

I would like to acknowledge a few individuals who have helped me to finish the work reported in this dissertation. I would like to thank my advisor Siyuan Han for his guidance and encouragement in the past several years. He also helped a lot in the experimental setup and initially suggested the measurement of LZS interferences in a coupled qubit-TLS system. I would also like to thank Guozhu Sun and Xueda Wen. Dr. Sun and I worked together to setup the experiment and managed to observe the LZS interference by precisely controlling the flux bias via the readout pulse line. The LZS interference pattern was measured by Guozhu Sun and most of the theoretical calculation was done by Xueda Wen. This work would not be possible without the collaborators at Northrop Grumman ES in Baltimore who fabricated the phase qubit and provided technical assistance. Rupert Lewis helped us in the setup of the microwave control unit and the measurement of spectroscopy. Finally, I thank all committee members for their support and helpful advice.

Chapter 1. Introduction

In the past decade, with the development of quantum computation theory including the discovery of quantum algorithms, researchers have been looking for candidate quantum objects to construct a quantum computer. Superconducting phase quantum bit (qubit) based on radio frequency (rf) superconducting quantum interference device (SQUID) is one of the most promising candidates. However, short coherence time (~ 10^2 ns) remains the main obstacle for the implementation of quantum computing using superconducting phase qubits despite the great efforts to investigate the mechanisms of decoherence and improve coherence time. One solution to the problem is to develop faster quantum gates. In this dissertation, a novel multi-partite quantum gates, realized by the precise coherent control of the quantum states via Landau-Zener (LZ) transitions, will be demonstrated in a phase qubit coupled to two microscopic two-level systems (TLSs). The results shows that this new approach increases gate speed significantly and is much simpler to implement, making it an important step toward the realization of quantum computers.

The content of this dissertation is organized as follows. In Chapter 1, the basics of quantum computing and its possible physical realization is introduced, followed by the discussion of the phase qubits based on rf SQUIDs. The qubit sample and experimental setup are described in Chapter 2. In Chapter 3, we discuss how to calibrate the parameters of the phase qubit and measure decoherence times. Chapter 4 presents the main experimental results from the coherent control of tripartite quantum states in a

coupled qubit-TLSs system via LZ transitions. The results will be summarized and discussed in chapter 5. The appendices for the supporting materials and technical details are placed after the bibliographic references.

1.1 Quantum computation

What is a quantum computer? Why do we need it?

The answer to the first question is quite straightforward: a quantum computer is a device which can perform computation using quantum mechanics. More precisely, it makes use of novel quantum phenomena such as superposition and entanglement.

The main reason for building quantum computers is that they allow us to solve certain problems exponentially faster than classical computers. Back into the 1980s, building computers based on the principles of quantum mechanics was first suggested by Richard Feynman to simulate quantum systems [1]. Later, David Deutsch attempted to define a universal quantum computer that would have more computational power than any classical computer [2]. Significant progress was made in 1994 when Peter Shor demonstrated two famous quantum algorithms for integer factorization and discrete logarithms [3]. Another important quantum algorithm for conducting the search through some unstructured space was discovered by Grover [4]. Because the speed for solving certain problems can be increased exponentially by using quantum algorithms, theoretical research on quantum computer continues with interests despite the difficulty in discovering new quantum algorithms. Meanwhile, remarkable progress has been made by many groups to realize the quantum computer via different quantum objects in the past decades. The details of the experimental approaches will be

presented in section 1.2 and 1.3.

1.1.1 Quantum bit

The basic element of a quantum computer is called "quantum bit" (qubit). Like a classical bit, it has two possible logic values, "0" or "1". However, for qubits the "value" here usually refers to the eigenvalue of a physical observable. Physically, a qubit is a quantum two-level system. The state of a single qubit could be an arbitrary superposition of the computational basis states $|0\rangle$ and $|1\rangle$. In practice, we usually choose the ground state of a qubit as $|0\rangle$ and the excited state as $|1\rangle$. In general, a pure qubit state $|\psi\rangle$ can be expressed in Dirac notation as

$$|\psi\rangle = \alpha|0\rangle + \beta|1\rangle, \qquad (1.1)$$

where α and β are complex numbers, and $\langle\psi|\psi\rangle = 1$, *i.e.*, $|\alpha|^2 + |\beta|^2 = 1$. If the same qubit state described by Eq. (1.1) is prepared before each measurement, then after a number of measurements the probability of finding the qubit in $|0\rangle$ and $|1\rangle$ would be given by $P_0 = |\alpha|^2$ and $P_1 = |\beta|^2$, respectively. More conveniently, the state described by Eq. (1.1) can be written as a vector in the form of a matrix $\begin{pmatrix} \alpha \\ \beta \end{pmatrix}$. Another useful representation of the single qubit state is to map the state to a unit vector on the Bloch sphere:

$$|\psi\rangle = \cos\frac{\theta}{2}|0\rangle + e^{i\varphi}\sin\frac{\theta}{2}|1\rangle \qquad (1.2)$$

where $0 \le \theta \le \pi$ is the angle between the state vector and the *z*-axis, and $0 \le \varphi < 2\pi$ denotes the angle between the state vector projected into the *x*-*y* plane and the *x*-axis, as shown in Fig. 1.1. Consequently, any single qubit can be mapped to a unique vector on the Bloch sphere, where the probability of finding the system in $|1\rangle$, also called the

excitation probability, is given by $P_1 = \left(\sin\frac{\theta}{2}\right)^2$. As an example, a vector located in the x-y plane corresponds to the state $\frac{1}{\sqrt{2}}\left(|0\rangle + e^{i\varphi}|1\rangle\right)$. Note that the variable φ is the other important degree of freedom, which gives the phase difference between the complex probability amplitudes α and β. Representing the qubit state by a Bloch vector is very useful in describing and visualizing the dynamics of a single qubit.

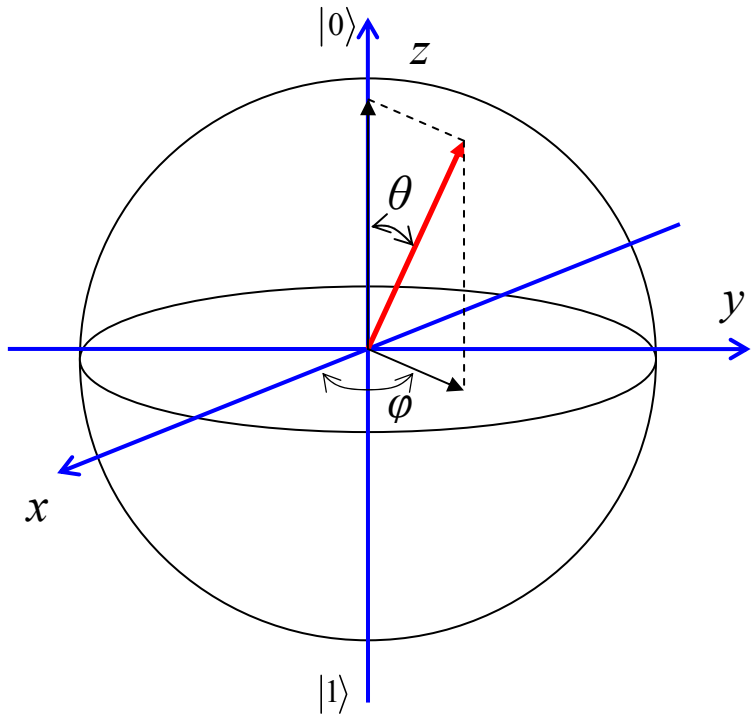

Fig. 1.1. A unit vector (in red) representing the qubit state on Bloch sphere.

1.1.2 Multiple qubits

A number of qubits can be coupled to each other to form a multiple-qubit circuit. Generally, for a system of N qubits, the computational basis states have the form $|x_1 x_2 \ldots x_N\rangle$, where $x_i = 0$ or 1. For simplicity, let's consider the simplest case: two coupled qubits A and B. The basis states for two qubits are $|00\rangle, |10\rangle, |01\rangle$, and $|11\rangle$.

Thus the state vector for any two qubits is given by

$$|\psi\rangle = a_1|00\rangle + a_2|10\rangle + a_3|01\rangle + a_4|11\rangle. \qquad (1.3)$$

As mentioned before, quantum entanglement is a novel feature of quantum systems having two or more qubits. To demonstrate quantum entanglement, consider one of the Bell states

$$|\Psi^+\rangle = \frac{1}{\sqrt{2}}(|01\rangle + |10\rangle). \qquad (1.4)$$

It can be shown that the Bell state $|\Psi^+\rangle$ can't be expressed as a direct product of two single qubit states, *i.e.*, $|\Psi^+\rangle \neq |\psi_A\rangle \otimes |\psi_B\rangle$. That means in the Bell state the two qubits A and B are not separable and thus *entangled*. As a consequence, the measurements of qubit A and B are fully correlated. Supposed a measurement of qubit A is performed and the result gives value "0" (or "1"). Then the Bell state will be collapsed to the state $|01\rangle$ (or $|10\rangle$). Hence, the following measurement of qubit B will *only* yield "1" (or "0"), as a result of quantum correlation.

1.1.3 Quantum gates

In the gate model quantum computing [5], the quantum computers are built from quantum circuits containing basic quantum logic gates, such as AND, OR, NOT, and CNOT. The quantum gates perform unitary transformations on qubit states. As an example, consider performing the NOT gate X on the qubit state $|\psi\rangle = \begin{pmatrix} \alpha \\ \beta \end{pmatrix}$, *i.e.*, $X|\psi\rangle = X\begin{pmatrix} \alpha \\ \beta \end{pmatrix} = \begin{pmatrix} \beta \\ \alpha \end{pmatrix} = |\psi'\rangle$, where $X = \begin{pmatrix} 0 & 1 \\ 1 & 0 \end{pmatrix}$. In addition, because the qubit state after any gate A is normalized as well, one has $A^\dagger A = I$, *i.e.*, the transformation is unitary.

When a single qubit has a time-independent Hamiltonian, *i.e.*, $\partial\hat{H}/\partial t = 0$, the evolution of the qubit state is simply given by $\left|\psi(\Delta t)\right\rangle = e^{-i\hat{H}\Delta t/\hbar}\left|\psi(0)\right\rangle$, where the propagator $\exp(-i\hat{H}\Delta t/\hbar)$ is a unitary transformation. As an example, for a qubit with $\hat{H} = -\frac{\hbar\omega}{2}\hat{\sigma}_z$, $\exp(-i\hat{H}\Delta t/\hbar) = \exp(i\omega\Delta t\hat{\sigma}_z/2) = R_{-z}(\omega\Delta t)$, where $\hat{\sigma}_z$ is the third Pauli matrix, and $R_{-z}(\omega\Delta t)$ is a rotation operator corresponding to a rotation of the state vector about the $-z$ axis by an angle of $\omega\Delta t$ in the Bloch sphere picture. Moreover, it is well known that an arbitrary single qubit operation U can be decomposed as a product of simple rotations about z and y axes. Consequently, all single qubit gates can be realized by a sequence of rotations.

Among the multiple-qubit quantum gates, the controlled-NOT (CNOT) gate is of particular interest because any multiple logic gate may be composed from CNOT and single qubit gates [5]. The CNOT gate has two input qubits, where one is the control qubit and the other is the target qubit. The operation of a CNOT gate can be described as follows. The state of the target qubit will be flipped when the control qubit is in $\left|1\right\rangle$, while the state of the target qubit will remain unchanged when the control qubit is in $\left|0\right\rangle$.

1.2 Physical qubits

As mentioned in section 1.1, a quantum computer must be a quantum object which is able to demonstrate novel quantum properties such as superposition and coherence. In practice, a quantum two-level system is desirable for the physical realization of qubits. More importantly, as a candidate for QC, a quantum system must satisfy a number of requirements as described below.

The critical requirements that a physical system must meet for QC are given by the so-called DiVincenzo criteria [6]:

1) Scalable physical system with well characterized qubits
2) Initialization to a simple fiducial state, such as $|0\rangle \otimes |0\rangle \otimes \cdots \otimes |0\rangle$
3) Long coherence time, much longer than gate operation time (~ 10^4-10^6 times)
4) Universal quantum gates
5) Measurement capability.

Unfortunately, many quantum systems would not be eligible according to these criteria. For instance, although long coherence time could be obtained in many microscopic systems which are well isolated from the environment, the isolation will also lead to insufficient coupling between the qubits or between the qubit and the control /measurement circuits. Furthermore, many systems are fundamentally not scalable, thus making it impossible to construct useful quantum computers from them.

With many candidate quantum systems considered and studied in the past decade, only a few appear promising for the purpose of scalable quantum computation. Among them are optical photons, trapped ions, and superconducting Josephson circuits.

Qubits can be realized by a single photon which has two optical modes. Optical photons do not interact strongly with the environment and are largely free of decoherence that plagues other systems. They can be guided along long distances and easily combined. Hence, the quantum coherence and entanglement is realized more easily. However, the large-scale optical elements widely used to construct the optical photon quantum computers are inherently not scalable [7, 8]. Only recently, the

potential of scalability has been demonstrated by building an integrated photonic circuit on a silicon chip [9].

Trapped ion qubits are another competitive approach. Isolated in an electromagnetic trap, the ions interact with laser beams [10]. The single qubits are stored in the internal states of the ions and the inter-qubit coupling is realized by the collective quantized motions of the ions. Lasers are applied for single-qubit operations and entanglements between the qubits. The advantages of trapped ion qubits are negligible decoherence and high measurement fidelity. Multiple-qubit entanglement has also been demonstrated in trapped ion qubits [11]. However, it remains challenging to make a surface trap based on integrated circuits for scalability [12, 13].

The last candidate introduced here is the superconducting qubits based on Josephson junctions. Among them is the rf SQUID qubits. In the following, we will focus the discussion on superconducting qubits, especially those based on rf SQUIDs.

1.3 Superconducting qubits

Unlike many other qubit systems, superconducting qubits are macroscopic in size (1 μm to 10^2 μm) and have macroscopic degree of freedoms [14, 15]. Basically, there are three types of superconducting qubits: charge qubit, flux qubit, and phase qubit. The macroscopic degrees of freedom for these three types of qubits are the number of Cooper pairs in a tiny superconducting island, the total magnetic flux in a SQUID loop, and the phase difference across a Josephson junction, respectively. Another interesting approach to QC using superconducting circuits is based on circuit quantum electrodynamics (QED), where the superconducting qubits are coupled to a microwave

cavity [16, 17]. All of these superconducting qubits utilize Josephson junctions as the key component.

A Josephson junction (JJ) consists of two superconductors separated by a thin insulating barrier as shown in Fig. 1.2 (a). Practically, the JJs commonly used in superconducting qubits are tunnel junctions with two superconducting thin films (~ 100 nm) separated by a thin oxide barrier (~ 1-2 nm).

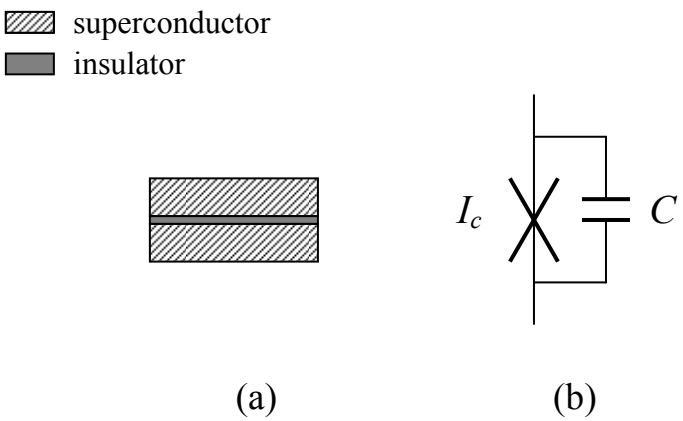

Fig. 1.2. Schematic of a Josephson tunnel junction (a), modeled as an ideal JJ (cross) shunted by a capacitor (b).

The electric current through the junction I and the voltage across the junction V are given by the Josephson relations [18]

$$I = I_c \sin\varphi \tag{1.5}$$

$$V = \frac{\hbar}{2e}\frac{\partial\varphi}{\partial t}, \tag{1.6}$$

where φ represents the wavefunctions' phase difference of the condensates of Cooper pairs in the two superconductors, and I_c is the critical current of the junction, *i.e.*, the magnitude of the maximum supercurrent through the junction. When the junction is

biased at $I < I_c$, it is a non-dissipative device with a nonlinear inductance equal to $\frac{\hbar}{2e}\frac{1}{I_c \cos\varphi}$, where $\hbar = h/2\pi$ is the reduced Planck's constant and e is the elementary charge. Note that the separated superconducting films also form a capacitor with the capacitance equal to C as shown in Fig. 1.2 (b). Therefore, a JJ can also be treated as a non-linear LC resonator. More importantly, the non-linearity will lead to anharmonicity in the potential energy of superconducting qubits, which allows one to construct effective two-level systems.

Basically, the variable φ describes the collective motion of the tunneling Cooper pairs and thus is a macroscopic degree of freedom. The energy associated with φ is called the Josephson coupling energy and is given by $-E_J \cos\varphi$, where $E_J = \frac{I_c \Phi_0}{2\pi}$ and $\Phi_0 = h/2e$ is the magnetic flux quantum. The other important variable to characterize a JJ is the charge Q on the junction, resulting in a charging energy $\frac{Q^2}{2C} = E_c N^2$, where N is the number of Cooper pairs and $E_c = \frac{(2e)^2}{2C}$. A charge qubit consists of a tiny superconducting island coupled by a Josephson junction to a superconducting reservoir. The charging energy is dominant $E_c \gg E_J$ in charge qubits while $E_c < E_J$ in flux qubits and phase qubits.

JJ was first proven to be a macroscopic quantum object by the demonstration of macroscopic quantum tunneling and energy level quantization in current biased JJs [19, 20]. In order to investigate JJ on the quantum level, the macroscopic variable φ has to be treated as an operator. Define $\hat{\Phi} = \frac{\hat{\varphi}}{2\pi}\Phi_0$ as the normalized phase difference, which is conjugate to the momentum operator $\hat{p}_\Phi = -i\hbar\frac{\partial}{\partial\Phi}$ with the commutation

relation $\left[\hat{\Phi}, \hat{p}_{\Phi}\right] = i\hbar$. According to the classical equation of motion (EOM) for the phase difference, a JJ can be treated as a particle of mass C [21]. Consequently, the Hamiltonian is given by

$$\hat{H} = \frac{\hat{p}_{\Phi}^{\ 2}}{2C} + U(\hat{\Phi}) \tag{1.7}$$

where U is the potential energy.

To derive the potential energy of a current biased JJ, consider a capacitively shunted JJ biased by a current I_b and assume damping from the environment is negligible. By using the Josephson relations in Eqs. (1.5) and (1.6), one obtains the EOM

$$C\frac{d^2\Phi}{dt^2} = I_b - I_c \sin\left(2\pi\Phi/\Phi_0\right) = -\frac{dU}{d\Phi}. \tag{1.8}$$

Hence, the potential U is given by

$$U(\Phi) = -I_b\Phi - E_J \cos(2\pi\Phi/\Phi_0). \tag{1.9}$$

When the two sides of a JJ are connected by a superconducting loop, forming an rf SQUID, the total magnetic flux threading the loop Φ_t is then related to the phase difference φ by the fluxoid quantization condition

$$\Phi_t + \frac{\varphi}{2\pi}\Phi_0 = n\Phi_0, \tag{1.10}$$

where n is an integer. Thus the total flux in the rf SQUID loop is also a macroscopic degree of freedom. It is much more convenient to choose the total flux as the dynamic variable when the rf SQUID is operated as a flux qubit. For convenience, hereafter we use Φ instead of Φ_t to represent the total magnetic flux threading the loop. Consider an rf SQUID having a loop inductance L and biased by an external

magnetic flux Φ_x. Hence, the potential energy of an rf SQUID is given by

$$U(\Phi) = \frac{(\Phi - \Phi_x)^2}{2L} - E_J \cos(2\pi\Phi / \Phi_0), \qquad (1.11)$$

where the first term comes from the magnetic energy stored in the rf SQUID loop.

Before discussing the details of superconducting qubits based on rf SQUIDs, we need to examine the features of superconducting qubits and evaluate them as a candidate for implementing quantum computing.

Compared to many other approaches, the most significant advantage of superconducting qubits is the sophisticated fabrication technology of superconducting integrated circuits. Superconducting devices are usually made on silicon wafers with advanced micro- and nano-fabrication techniques, such as optical or electron beam lithography and thin film deposition. The circuit elements include tunnel junctions, capacitors, and inductors, all of which are connected by superconducting wires and transmission lines. Hence, the design is very flexible and the circuits can be highly scalable.

Second, the coupling between qubits or between a qubit and its control and readout circuits is tunable and can be designed to be sufficiently strong. For instance, the total flux in a qubit loop could be manipulated by an on-chip loop inductively coupled to the qubit. However, on the other hand, the macroscopic degree of freedom of the qubit also couples to the parasitic environmental modes and noise, thus inducing decoherence.

In order to use JJ-based devices as qubits, the devices must be cooled down to low temperatures. Below the critical temperature of superconductors, JJs become

non-dissipative. Furthermore, the thermal fluctuation energy $k_B T$ needs to be much less than the energy level spacing between the qubit states $\Delta E_{10} = \hbar\omega_{10}$, where k_B is Boltzmann's constant. The typical value of $\omega_{10}/2\pi$ is in the range of 5 - 20 GHz, corresponding to 0.25 - 1 K. Thus to make the effect of thermal fluctuation negligible, the qubits must be cooled down to ultra low temperatures (~ 20 mK), which is accessible using a dilution refrigerator.

1.4 Superconducting qubits based on rf SQUIDs

After the demonstration of macroscopic quantum tunneling (MQT) in current-biased JJs [20], more fascinating macroscopic quantum phenomena were observed in JJs and rf SQUIDs. Among them are macroscopic resonant tunneling (MRT), photon-assisted tunneling (PAT), photon induced transition (PIT), and quantum superposition of macroscopic states [22-27]. The macroscopic quantum coherence (MQC) in the time domain was first observed in a charge qubit [28]. Subsequently, MQC was also successfully demonstrated in JJ phase qubits and 3-JJ flux qubits [29-31]. With a fast readout scheme and improved design and fabrication technology, the phase qubit based on large inductance rf SQUID has been developed to be one of the leading candidates among the superconducting qubits [32-36]. In comparison, the pursuit of an rf SQUID flux qubit has encountered considerable difficulties in observing MQC in the time domain [26]. The same amount of magnetic flux noise would result in much stronger decoherence in an rf SQUID operated as a flux qubit instead of as a phase qubit. The resulting dephasing rates in the rf SQUID when operated as flux or phase qubit will be shown in subsection 1.5.2.

1.4.1 Properties of rf SQUID

In general, the size of rf SQUID qubits (≥ 50 μm) is 10 to 10^2 times larger than that of charge qubits and 3-JJ flux qubits. The larger size allows higher fabrication yield and stronger coupling between the qubits. Physically, an rf SQUID can be inductively coupled to an external flux bias circuit (control) and a dc SQUID (readout), as shown in Fig. 1.3 (a). The basic parameters of an rf SQUID include the junction critical current I_c, junction capacitance C, and the SQUID loop inductance L. The Hamiltonian is fully determined by those three parameters and thus an rf SQUID qubit can be considered as an artificial atom.

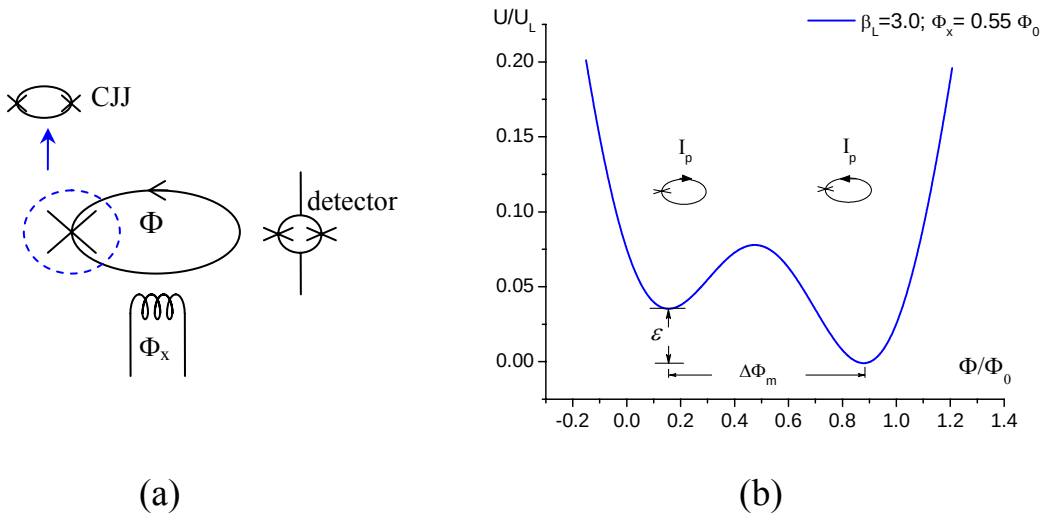

Fig. 1.3. Schematic of an rf SQUID coupled to the control and readout lines, where the single JJ could be replaced by a compound JJ for a tunable effective critical current (a), and a typical double-well potential at β_L=3 and Φ_x=0.55 Φ_0 (b).

A very useful variation of the traditional rf SQUID is the compound Josephson junction (CJJ) rf SQUID, where the single junction is replaced by a small dc SQUID with inductance $L_{dc} << L$. Thus the critical current of the CJJ can be adjusted *in situ*

by applying a magnetic flux to the dc SQUID [37].

By defining the parameter $\beta_L = \frac{2\pi L I_c}{\Phi_0}$, the rf SQUID potential given in Eq. (1.11) can be written as

$$U(\Phi) = \frac{\Phi_0^{\ 2}}{L}\left[\frac{1}{2}\left(\frac{\Phi - \Phi_x}{\Phi_0}\right)^2 - \frac{\beta_L}{4\pi^2}\cos(2\pi\Phi/\Phi_0)\right] \qquad (1.12)$$

where the first term is the magnetic energy stored in the loop inductor and the second is the Josephson coupling energy. The shape of the potential is determined by the external flux bias Φ_x and β_L, while the energy scale is given by $U_L = \Phi_0^{\ 2}/L$. When $1 < \beta_L < 4.6$, the potential is a symmetric double-well potential at $\Phi_x = \Phi_0/2$. By increasing the flux bias slightly by $\delta\Phi_x$, the left well will be higher than the right and the energy difference between the two potential minima is given by $\varepsilon \cong 2I_p\delta\Phi_x \approx \Delta\Phi_{\mathrm{m}}\delta\Phi_x/L$, where I_p is the magnitude of the circulating current in the rf SQUID loop and $\Delta\Phi_{\mathrm{m}}$ is the distance between the two potential minima, as shown in Fig. 1.3 (b). Note that when the system is localized in either the left or right well, the corresponding I_p is either clockwise or counterclockwise, which can be measured by a detector, such as an inductively coupled dc SQUID magnetometer.

Given the Hamiltonian described in Eq. (1.7), one can solve the corresponding one-dimensional stationary Schrödinger equation to obtain the energy eigenvalues and eigenstates. It turns out that many eigenstates are localized in the wells when the barrier height is much greater than the energy level spacing between the lowest two levels in the same well. In the same well, the energy level spacing between adjacent levels decreases at higher levels due to the anharmonicity of the potential. Furthermore,

the energy level spacing between the intra-well ground state and first excited state $\hbar\omega_{10}$ is on the order of $1/\sqrt{LC}$, typically 5 – 20 GHz. A typical energy level diagram of an rf SQUID is shown as an example in Appendix C.

1.4.2 Dynamics of a phase qubit under microwave radiation

In the gate model QC, microwave pulses are applied to rf SQUID qubits to perform quantum gate operations. Consider the microwave as a classical electromagnetic field described by $A_{rf}\sin\omega t$, where A_{rf} is the amplitude and ω is the angular frequency of microwave. Because the linear dimension of the qubit (~ 0.1 mm) is much smaller than the wavelength of the microwave (~ 1 cm), the spatial variation of the field is negligible. The microwave will generate an rf magnetic flux $\Phi_{rf}\sin\omega t$ in the SQUID loop, where Φ_{rf} is proportional to the microwave amplitude A_{rf}. From Eq. (1.11), one can find that the interaction Hamiltonian is given by $H_I = -I_{rf}\sin\omega t\hat{\Phi}$, where $I_{rf} \equiv \frac{\Phi_{rf}}{L}$. By using an IQ mixer, the microwave can have both in-phase (I) and quadrature (Q) components, *i.e.*, $A_1\sin\omega t + A_2\cos\omega t$, where the amplitudes A_1 and A_2 are adjustable.

To operate the rf SQUID as a qubit, the qubit states $|0\rangle$ and $|1\rangle$ need to be specified. For phase qubits, the ground and first excited states localized in the same well are used as the qubit states. In contrast, a flux qubit utilizes the ground and first excited states of the double-well potential around $\Phi_x = \Phi_0/2$. With a "moderate" height barrier between the two wells, the qubit states could be "partially" localized in the wells. For both types of rf SQUID qubits excited by a resonant microwave, the coupling between the qubit states is dominant, while the coupling to the other states is

negligible thanks to the anharmonicity of the potential. Hence, an effective two-level system is obtained.

The dynamics of a qubit under microwave radiation is determined by the system Hamiltonian. Consider the Hamiltonian of a phase qubit first (refer to Appendix A for the details of the derivation). Write the total Hamiltonian as $H = H_0 + H_I$, where $H_I = -I_{rf} \sin \omega t \hat{\Phi}$. Choose the qubit states $|0\rangle$ and $|1\rangle$ as the basis states and thus $\hat{H}_0 = -\frac{\hbar\omega_{10}}{2}\sigma_z$. To calculate the matrix elements of operator $\hat{\Phi}$, use the fact that the potential is approximately harmonic around the bottom of a deep well, where the barrier height is much greater than $\hbar\omega_{10}$. Thus $\hat{\Phi} = \Phi_{01}\sigma_x$, where $\Phi_{01} = \langle 0|\hat{\Phi}|1\rangle$. In order to obtain a time-independent Hamiltonian, the rotating wave approximation (RWA) can be applied when the detuning $\Delta\omega = \omega_{10} - \omega \ll \omega_{10}$. Consequently, in the ω rotating frame (rotating about the *z*-axis), the Hamiltonian is given by

$$\hat{H} = -\hbar\left(\Delta\omega\frac{\sigma_z}{2} + \Omega_0\frac{\sigma_y}{2}\right), \tag{1.13}$$

where the angular frequency of the on-resonance Rabi oscillation, $\Omega_0 = \sqrt{\frac{1}{2C\hbar\omega_{10}}}I_{rf}$, is proportional to the microwave amplitude.

The Hamiltonian given in Eq. (1.13) corresponds to a rotation operation on the qubit state vector. As mentioned before, when the system's Hamiltonian is time-independent, the state vector is given by $|\psi(\Delta t)\rangle = e^{-i\hat{H}\Delta t/\hbar}|\psi(0)\rangle$. The effective two-level Hamiltonian of the qubit can be always expressed in the general form of $\hat{H} = \hbar\Omega\frac{\vec{n}\cdot\vec{\sigma}}{2}$, where $\vec{\sigma} = (\sigma_x, \sigma_y, \sigma_z)$ and $\vec{n}$ is a unit vector. So the propagator is given by $\exp\left(-i\Omega\Delta t\frac{\vec{n}\cdot\vec{\sigma}}{2}\right) = R_{\vec{n}}(\Omega\Delta t)$, equivalent to a rotation of the

state vector about $\vec{n}$ with the angular frequency Ω by an angle $\Omega\Delta t$. Hence, the Hamiltonian in Eq. (1.13) corresponds to a rotation of the state vector about a unit vector $\vec{n} = \left(0, -\frac{\Omega_0}{\Omega}, -\frac{\Delta\omega}{\Omega}\right)$, where $\Omega = \sqrt{\Omega_0^{\ 2} + (\Delta\omega)^2}$ is the angular frequency of Rabi oscillation.

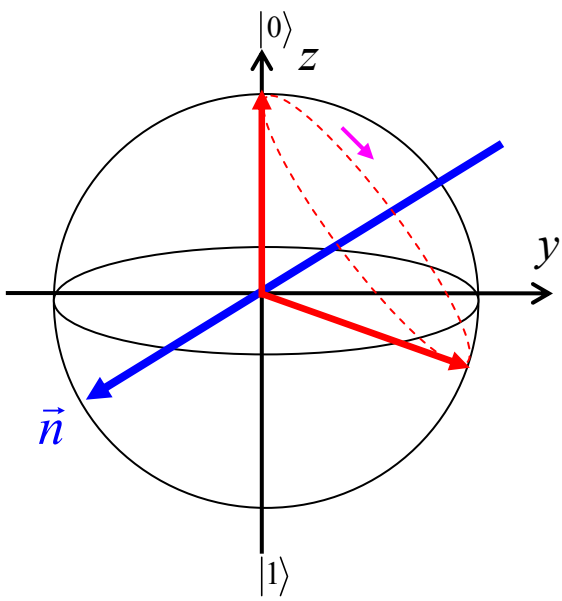

Fig. 1.4. Operation of phase qubit state vector using microwave pulses. The system Hamiltonian is given in Eq. (1.13). The qubit is initialized in the ground state. Under microwave excitation, the state vector (red) is rotating about the unit vector (blue) determined by detuning and on-resonance Rabi frequency.

Fig. 1.4 demonstrates such a rotation when the qubit is initially prepared in the ground state. A microwave pulse of a duration Δt is called a π/2-pulse or π-pulse when $\Omega\Delta t = \pi/2$ or π. Furthermore, when the microwave has both the in-phase and quadrature components with $H_I = (I_1 \sin\omega t + I_2 \cos\omega t)\hat{\Phi}$, the qubit Hamiltonian has an extra term $-\hbar\Omega_{02}\frac{\sigma_x}{2}$, where $\Omega_{02} \propto I_2$. Thus the rotation about the x-axis can be realized as well. The rotation of the qubit state vector will result in a periodic

oscillation in the excitation probability $P_1 = \left(\sin\frac{\theta}{2}\right)^2$. For on-resonance Rabi oscillations, with $|\psi(0)\rangle = |0\rangle$, we have $\theta = \Omega_0 t$ and

$$P_1(t) = \frac{1-\cos\Omega_0 t}{2}. \tag{1.14}$$

For rf SQUID flux qubits, in the basis of qubit eigenstates, the flux qubit Hamiltonian has essentially the same form as that of phase qubits. However, the basis states are conventionally chosen to be a combination of the qubit states. For instance, at $\Phi_x = \Phi_0/2$, the basis states are actually the lowest states localized in each of the wells $|R\rangle = \frac{1}{\sqrt{2}}(|0\rangle + |1\rangle)$ and $|L\rangle = \frac{1}{\sqrt{2}}(|0\rangle - |1\rangle)$. Thus the flux qubit Hamiltonian before the RWA is expressed as $\hat{H} = -\frac{1}{2}(\varepsilon\sigma_z + \Delta\sigma_x)$, where $\varepsilon \propto \Phi_{rf}\sin\omega t$ and Δ is the tunnel splitting. Thus it is equivalent to the Hamiltonian of a phase qubit.

1.5 Decoherence in rf SQUID qubits

As a macroscopic quantum object, an rf SQUID qubit is subject to considerable decoherence resulting from its relatively strong coupling to the environment. In general, decoherence in a qubit is related to two processes: the longitudinal relaxation with decay rate $1/T_1$ and the transverse relaxation with decay rate $1/T_2$, where T_1 and T_2 are also called the energy relaxation time and dephasing time, respectively. Here we explain how decoherence occurs in phase qubits using the concept of qubit "particles". In general, the occupation probabilities of qubit states are determined by performing a number of measurements ($N \sim 10^4$) with the same initialization and gate operations. Essentially, it is equivalent to performing measurements on an ensemble of N qubit "particles". Thus the process of the longitudinal or energy relaxation could be

described as follows. At first, each qubit particle is prepared in the ground state and brought to the excited state by a π-pulse. Then due to the dissipation, some qubit particles would dump energy to the environment and decay to the ground state. After time *t*, the number of qubit particles remaining in the excited state is given by Ne^{-t/T_1}.

To describe the transverse relaxation or dephasing process, consider first an operation taking the state vectors of the qubit particles into the *x*-*y* plane of the Bloch sphere. Then the state vectors are allowed to evolve freely so that they will rotate about the *z*-axis in the *x*-*y* plane with the angular frequency $\Delta E_{10}/\hbar$, where ΔE_{10} is the energy level spacing between the qubit states. However, in the presence of dephasing during the free evolution, the state vectors of some qubit particles rotate randomly faster or slower, which randomizes the phase difference between the qubit particles. In order to measure the effect of dephasing, a π/2-pulse following the free evolution is required to bring the state vectors into *y*-*z* plane and subsequently the measurement of state vectors' *z*-component is performed. The measured excitation probability P_1 is a damped sinusoidal oscillation as a function of free evolution time, *i.e.*, the signal of Ramsey fringes. The time constant of the amplitude decay is defined as the decoherence time T_2. Note that the energy relaxation also contributes to dephasing because it reduces the population of the "coherent" particles in the ensemble. Conventionally, the dephasing rate can be written as [38]

$$\frac{1}{T_2} = \frac{1}{2T_1} + \frac{1}{T_\varphi} \qquad (1.15)$$

where $1/T_\varphi$ represents the pure dephasing rate. In Eq. (1.15), it is assumed that the behavior of pure dephasing can be described by an exponential decay, *i.e.*,

$\exp\left(-t/T_{\varphi}\right)$. However, the decay is non-exponential in rf SQUID qubits. Actually, it will be shown in Chapter 3 that the coherence signal of an rf SQUID phase qubit decays as $\exp\left[-\left(t/T_{\varphi}\right)^2\right]\exp\left(-t/2T_1\right)$.

In rf SQUID qubits, the energy level spacing of the qubit states depends on the magnetic flux bias and thus it will fluctuate in the presence of flux noise, leading to inhomogeneous dephasing during the free evolution of the qubit state. To estimate in which frequency range the flux noise could cause inhomogeneous dephasing, consider a number of 10^4 measurements with the time interval between two consecutive measurements typically on the order of 1 ms. Hence, the flux noise with frequency as low as 0.1 Hz will contribute to dephasing. Fortunately, dephasing due to the low frequency flux noise could be significantly reduced by using the spin echo pulse sequence. The details of Ramsey fringe and spin echo measurements will be presented in Chapter 3.

1.5.1 RF SQUID qubits coupled to the environment

The superconducting qubits, including the rf SQUID qubits, are coupled to the electromagnetic environment. The qubit energy is dissipated to the environment and thus the lifetime of the excited state is limited by the energy relaxation. On the phenomenological level, the electromagnetic environment could be modeled as an effective frequency-dependent impedance $Z(\omega)$ in parallel with the qubit [39, 40], where the dissipation is induced by the damping resistor with an effective damping resistance $R = 1/\mathrm{Re}\left[Z(\omega)^{-1}\right]$. By noting that a JJ is a non-linear resonator, one could model a JJ phase qubit coupled to the environment as a parallel RLC circuit, where the

energy stored in the LC resonator is dissipated in the resistor, as shown in Fig. 1.5.

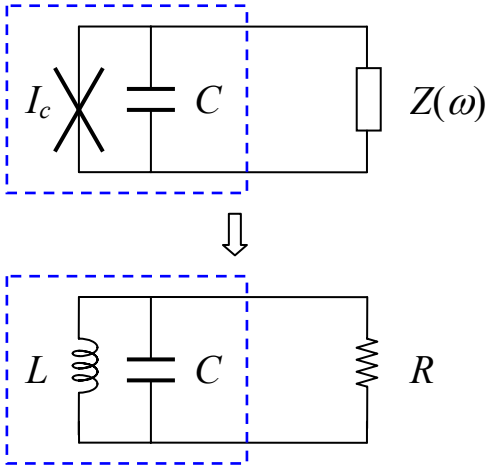

Fig. 1.5. Equivalent RLC circuit representation of a JJ coupled to the environment.

The energy loss in a classical parallel RLC circuit is characterized by the quality factor $Q = R\sqrt{\frac{C}{L}}$. In addition, when $Q >> 1$, the time constant of the circuit is approximately equal to $2RC$, corresponding to an energy relaxation time $T_1 = RC$. Intensive theoretical work has been done to investigate quantum dissipative systems based on the system-plus-reservoir model, where the bath is considered linear and described by harmonic oscillators [41-43]. In particular, for an rf SQUID flux qubit with ohmic dissipation, it has been predicted that coherent oscillation in the qubit could be destroyed when the dimensionless damping parameter $\frac{(\Delta\Phi_m)^2}{2\pi\hbar} R > \frac{1}{2}$ [44], where $\Delta\Phi_m$ is the distance between the bottoms of the two wells. Thus the damping resistance is an important parameter of the system and it could be determined by measuring the quality factor Q [45].

1.5.2 Low frequency magnetic flux noise

Consider the state vector of an rf SQUID qubit, which is prepared in the *x*-*y* plane and allowed to evolve freely. The angular frequency of the rotation about the *z*-axis is $\omega_{10} = \Delta E_{10} / \hbar$, where the energy level spacing of the qubit ΔE_{10} is determined by the qubit parameters and the external magnetic flux bias Φ_x. In the presence of flux noise, the instantaneous angular frequency could be written as $\tilde{\omega}_{10} = \omega_{10} + \frac{\partial \omega_{10}}{\partial \Phi_x} \delta\Phi_N$, where $\delta\Phi_N$ represents the magnetic flux noise. We will show later that the pure dephasing rate is given by $1/T_\varphi = \frac{\partial \omega_{10}}{\partial \Phi_x} \Delta\Phi_N / \sqrt{2}$, where $\Delta\Phi_N$ is the root mean square (rms) of the flux noise. To estimate the effect of pure dephasing, consider a typical rf SQUID qubit with the loop inductance L = 1 nH, qubit capacitance C = 100 fF, and $\beta_L = 2$. If it is operated as a phase qubit, then $\frac{\partial \omega_{10}}{\partial \Phi_x} \approx 2\pi \times 70\ \text{MHz/m}\Phi_0$. Given that the rms of flux noise is typically on the order of $0.1\,\text{m}\Phi_0$, one obtains $T_\varphi \sim 30\ \text{ns}$. However, when the rf SQUID is operated as a flux qubit, the energy level spacing is much more sensitive to the flux bias, where $\frac{\partial \omega_0}{\partial \Phi_x} \sim 2\pi \times 3.5\ \text{GHz/m}\Phi_0$. That yields a much shorter dephasing time $T_\varphi \sim 0.6\ \text{ns}$.

The spectral density of magnetic flux noise in superconducting qubits has been found to scale as 1/*f* at low frequency, and the typical flux noise at 1 Hz $S_\Phi^{1/2}(1\,\text{Hz})$ is on the order of $10^0 - 10^1\ \mu\Phi_0 / \sqrt{\text{Hz}}$ [46-49]. Thus the inhomogeneous dephasing in rf SQUID qubits is largely caused by the low frequency flux noise. In addition to dephasing, the low frequency flux noise also results in inhomogeneous broadening of

the MRT and microwave absorption resonance peaks. Recently, several theoretical models have been suggested to identify microscopic origins of low frequency flux noise [50-52]. In general, the magnitude of flux noise does not have a simple dependence on the area enclosed by the qubit loop. Instead, it was found to increase with $\sqrt{l/w}$, where l and w are the length and width of the superconducting wire respectively, indicating that the source of the noise is local [48]. Recent experiment has shown that unpaired spins in the superconducting film could generate $1/f$ magnetic flux noise and the area density of the unpaired spins is on the order of 0.4 spins/nm^2 [53].

Chapter 2. Qubit samples and experimental setup

2.1 Sample fabrication

The superconductors used to make superconducting qubits are typically Al or Nb deposited on silicon or sapphire substrates. Josephson junctions in many Al-based qubits are fabricated by angle shadow evaporation [27, 28]. The other approach to fabricate Al/AlO_x/Al junction is using an ion-mill cleaning followed by the thermal oxidation of the Al base electrode and the sputtering of the counter electrode [54]. The Al phase qubit we measured was made from a tri-layer process at Northrop Grumman [55]. Compared to the shadow evaporation technique, the tri-layer process provides more flexibility in qubit design and is thus more suitable for scalable quantum computing.

2.2 Qubit samples and designs

An Al qubit chip is illustrated in Fig. 2.1. It was made on a silicon substrate. The qubit has single tunnel junction with the junction area of 4.6 μm^2. As shown in the figure, the rf SQUID has a multi-turn structure, which provides adequate loop inductance. The dc SQUID magnetometer is between the rf SQUID and the other multi-turn structure with the identical geometry. Separate low frequency and high frequency flux bias lines are placed near the rf SQUID to produce sufficient couplings. The symmetric design minimizes the crosstalk between the flux bias lines and the dc SQUID. Because flux noise level in Al rf SQUID qubits is generally lower than that in Nb qubits, Al qubits are more suitable for the gate model quantum computing and are

often operated as phase qubits to reduce the dephasing rate. The connectors and cables we used for the microwave transmission have a cutoff frequency of 18 GHz. Hence, the transition frequency of our phase qubits $\Delta E_{10}/h$ is typically designed to be 5 - 18 GHz. The parameters of the Al phase qubit can be determined from the measurement of qubit spectroscopy, which will be shown in Chapter 3.

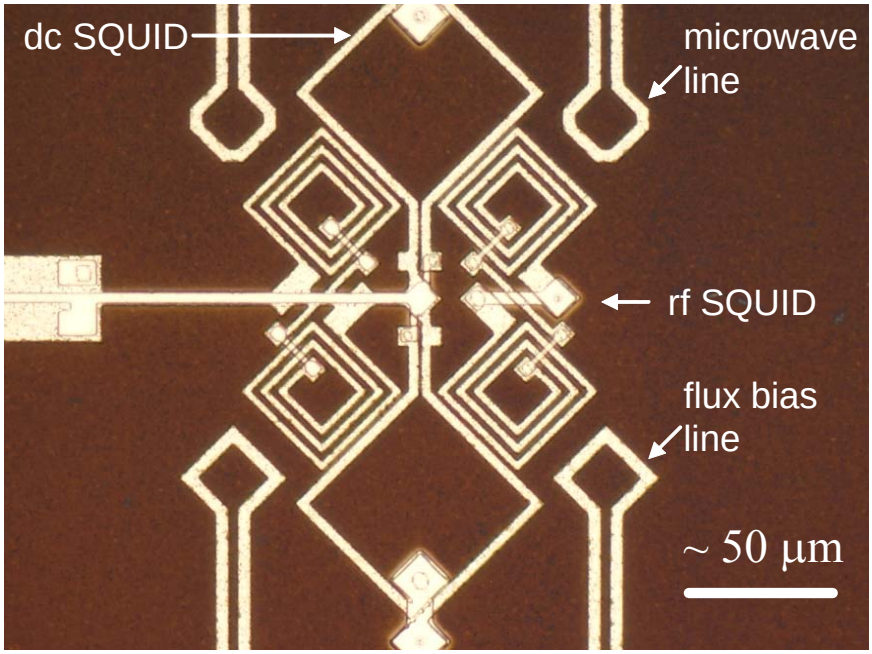

Fig. 2.1. Photomicrograph of an Al qubit sample deposited on silicon substrate: rf SQUID (the multi-turn structure on the right), dc SQUID magnetometer (the large double-loop structure in the center), microwave line and flux bias line (the small loops).

To design a superconducting qubit based on rf SQUID, several important parameters need to be considered. As introduced in Chapter 1, an rf SQUID is characterized by three parameters: the junction critical current I_c, the junction capacitance C, and the rf SQUID loop inductance L. The junction critical current I_c is given by the product of the critical current density J_c and the junction area A while

the junction capacitance $C \propto A$. J_c is determined by the thickness of the AlO_x tunnel barrier, which is typically ~ 1-2 nm and yielding J_c ~ 1-100 A/cm^2. The size of the junction is on the order of 1 μm. The rf SQUID loop inductance depends on its geometry and can be modeled accurately by using software such as FastHenry. Note that inductance scales with the dimension of the device and the flux bias lines are inductively coupled to the target elements of the qubit circuit. Hence, the mutual inductances between various circuit elements, which determine the coupling strength, need to be modeled when designing the qubit circuit.

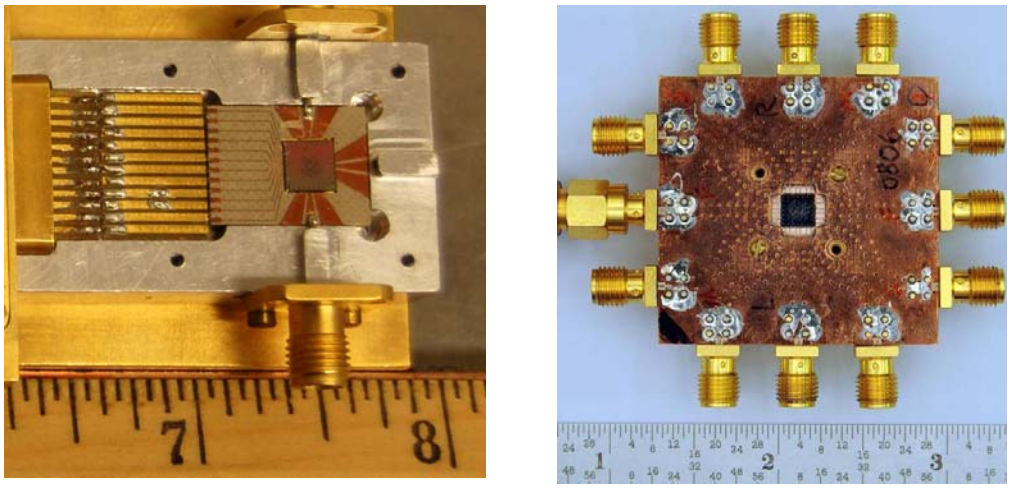

(a) (b)

Fig. 2.2. Sample cells: (a) Nb rf SQUID sample and (b) Al rf SQUID sample. The scales shown in both photos are in units of inch.

2.3 Sample packages

According to the type and size of the qubit chip, a special sample cell or chip carrier was used to hold a qubit chip for wiring the chip to external circuits. In Fig. 2.2 (a), we show a Nb qubit chip mounted in an aluminum sample cell. The qubit chip was

attached to an oxygen-free copper block by a thin layer of GE varnish, which provides thermal contact between the chip and the thermal bath at low temperatures (~ 20 mK). Then the chip and the copper block were enclosed in an aluminum box which provides additional magnetic shielding below aluminum's critical temperature (about 1.2 K). The cover of the Al box is not shown in the figure. Parts made from oxygen-free copper were gold plated for corrosion prevention.

To connect the qubit to the external electrical circuits for qubit control and readout, wire bonding is needed. We use the ultrasonic wire-bonding machine Kulicke&Soffa 4526 with 0.05 mm Al bonding wires. The wire bonding is probably the most delicate part in the preparation of the sample package. The bonding must be durable because the bonded wires will be subject to the tension induced by thermal contraction when cooled down from room temperature to low temperatures. The quality of wire bonding depends on several conditions including the material and surface condition of the sample, and the temperature and humidity of the environment. In addition, great care has to be taken when bonding to dc SQUID magnetometers. Because the critical current of dc SQUIDs is on the order of 1 μA, they are quite easy to be damaged by electrostatic discharge. To protect the dc SQUIDs, all the leads of each dc SQUID were connected to ground via 10 MΩ resistors. Coplanar transmission lines in the sample package are also shown in Fig. 2.2 (a). The transmission lines are formed by copper traces on the dielectric substrate. Two of the transmission lines for high frequency signals were connected to the top and bottom SMA connectors. Fig. 2.2 (b) shows the sample package of an Al phase qubit where all the transmission lines are

connected to SMA connectors. The characteristic impedance of these transmission lines are designed to be 50 Ω to minimize reflection.

2.4 Filtering and shielding

Experiments on superconducting qubits are quite challenging, where an ultra-low noise environment and very sensitive measurements of qubit states are required. The electrical and magnetic noise from the external control and readout circuit would either cause significant decoherence or even overwhelm the qubit signals. Therefore, the electrical leads connected to the qubits need to be properly filtered and attenuated, and the qubit samples must be adequately shielded.

Except for the microwave line, the external qubit control and readout lines have a bandwidth up to 1 MHz, filtered by low-pass RC, LC, and copper powder filters placed at cryogenic temperatures. To eliminate high frequency external noise, a home-made integrated LC copper powder filter (CPF) was engineered. The LC-CPF has a cut-off frequency of about 5 MHz and provides more than 90 dBm attenuation at the frequency greater than 400 MHz. The detail of the design and test of the LC-CPF can be found in Appendix B. The bandwidth of the microwave line is up to 18 GHz, limited by the bandwidth of the microwave cables and the SMA connectors. To reduce the noise in the microwave line, a dc block was used to block low frequency noise from room temperature and attenuators were installed.

With the control and readout circuits adequately filtered and attenuated, great efforts were also taken to improve the electrical and magnetic shielding of the system. The materials used to construct the sample cell are non-magnetic. The Al or Nb sample

cell box provided excellent magnetic shielding below 1 K. The sample package was anchored to the bottom of a dilution refrigerator. The inner and outer vacuum cans of the fridge were enclosed in a Cryoperm cylinder at 4.2 K and a Mu-metal cylinder at room temperature respectively to further enhance the magnetic shielding. The residual magnetic field in the sample cell was found on the order of 50 nT [56], indicating an excellent magnetic shielding. For electrical shielding, the dilution fridge and the battery-powered low-noise preamplifier/isolation amplifiers were placed in a shielding room. Coaxial and twin-axial cables with excellent shields were used to carry the signals. The electromagnetic noise picked up by the shields was guided to a separate customized ground, which is much more stable than the electrical ground of the lab building. In addition, isolation amplifiers were used to eliminate the ground loops in the circuits.

2.5 Experimental setup

The complete experimental setup to measure the Al phase qubit is illustrated in the schematic drawing of Fig. 2.3 (a). The sample package was mounted onto the mixing chamber of the dilution fridge, where the base temperature is about 20 mK. In the figure, different colors are used to distinguish the flux bias lines, the readout lines, and the microwave line. All these lines were single-ended. The copper powder filters (CPFs) were made from Mini Circuit 80-MHz LC low-pass filters filled with copper powder. They were installed in the flux bias lines and the readout lines, and were thermally anchored to the mixing chamber. The RC filters (RCFs) anchored to the 1 K pot (T = 1.4 K) have the cutoff frequency of up to several hundred KHz. Its design

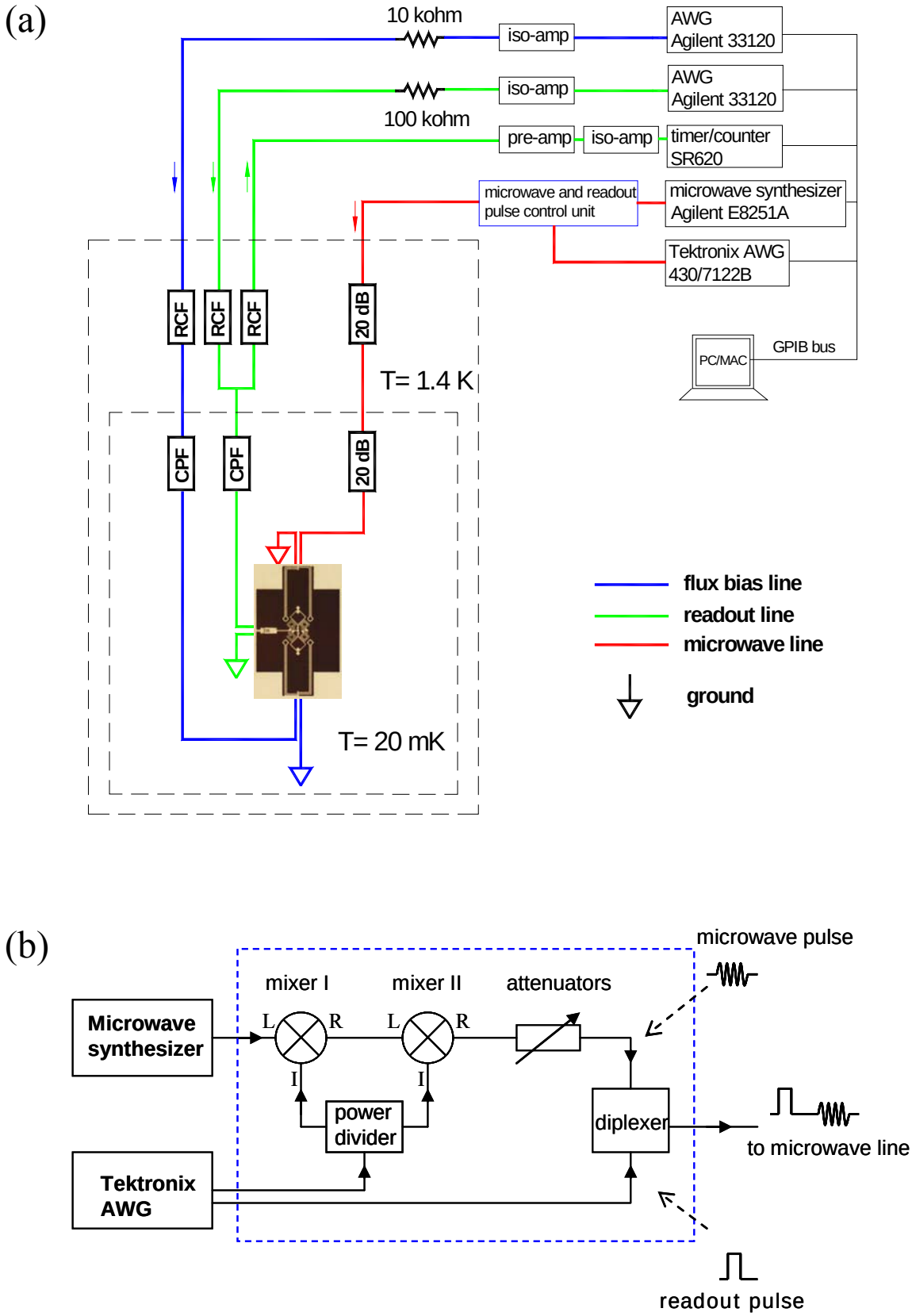

Fig. 2.3. (a) Schematic drawing of the experimental setup, where copper power filters (CPFs), RC filters (RCFs), and attenuators were anchored at low temperatures. (b) The microwave and readout pulse control unit (in blue box), where double mixers were

used to obtain up to 47 dB on-off ratio in the generated microwave pulse. Refer to section 2.5 for more details.

is shown in Appendix B. One of the readout lines (in green) was for the current bias of the dc SQUID magnetometer and the other one was used to measure the voltage across the dc SQUID. At room temperature, bias resistors of 10 kΩ and 100 kΩ were used to reduce the noise current in the flux and dc SQUID bias lines, respectively. Three isolation amplifiers were placed in those lines to break the ground loops in the circuits. The amplifiers have been tested to have a bandwidth of up to several 100 kHz. The arbitrary waveform generators (AWGs) of Agilent 33120 were used to bias the dc SQUID and the flux lines. The voltage signal from the dc SQUID was first amplified by a pre-amplifier (e.g., an AD524 instrumentation amplifier) and then measured by a SR620 timer. All instruments were connected to computers via a GPIB bus and programmed to be controlled.

The microwave line inside the fridge was attenuated by 40 dBm. At low temperatures, a semi-rigid coaxial microwave cable of about 2 meters long was used to carry both the microwave and readout pulses. The inner material of the cable is BeCu and the outer is stainless steel (SS). The cable itself will provide about 12 dBm attenuation at 10 GHz. At room temperature, the microwave line consisted of a 2.5 m low-loss simi-rigid copper coaxial cable. To reduce the low frequency noise from the room temperature components, a dc block with a passing band of 10 MHz to 18 GHz was installed. The microwave line was connected to an Agilent E8251A microwave synthesizer and high speed Tektronix AWGs (430 and 5014A or 7122B) via the control unit. The microwave source is able to generate microwave signal with frequency up to

20 GHz and power level up to 20 dBm. The high speed Tektronix AWG 430 and 7122B (5014A) have the sampling rate up to 0.2 and 12 (1.2) giga samples per second (GS/s), sufficient for generating readout pulse and microwave gate pulse, respectively. The setup of the microwave and readout control unit is shown in Fig. 2.3 (b). The microwave synthesizer outputs continuous microwave while the microwave pulse is generated by two double-balanced mixers (M/A-com M79HC) connected in series. The high resolution (≤1 ns) gate pulse from the Tektronix AWG 7122 B (or 5014A) was first divided by a power divider (Pico-second 5331) and then was fed into the mixers' intermediate frequency (IF) port (labeled "I"). The microwave pulse width is determined by the duration of gate pulse when the on-off ratio is high. Therefore, we used double mixers to enhance the on-off ratio to 47 dB, sufficient for generating accurately defined microwave pulses. The microwave pulse was then attenuated by attenuators (Midwest ATT-0290). Subsequently, the microwave pulse was combined with the readout pulse by a diplexer (Reactel 2SMX-2G-00) and fed to the qubit through the microwave line. The readout pulse is also generated by the Tektronix AWG and the duration of the pulse is about 5 ns.

Another critical issue for the setup is how to thermally ground the qubit chip. Although the sample cell is thermally anchored on the mixing chamber at 20mK, the local temperature of the qubit chip could be much higher due to the heat conducted from the qubit control and readout lines. Notice that superconductors in the superconducting state are excellent thermal insulators. Hence, we used the GVL flexible superconducting coaxial cables, which have excellent electrical conductance

and minimum thermal conductance, for the flux bias and readout lines below the 1 K pot. Each of the 1.5-meter superconducting cables is made of NbTi with a CuNi shield and has a cutoff frequency of up to several hundred MHz. From 1.4 K to room temperature, GVL brass coaxial cable was used in all low frequency lines because of its small temperature-coefficient of resistance. The shields of both the superconducting and brass cables were well anchored onto various thermal sinks. For the microwave line, the semi-rigid BeCu coaxial cable was anchored to 1 K pot and mixing chamber via 20 dB attenuators, respectively.

Chapter 3. Calibrating qubit parameters and decoherence time

In order to precisely manipulate multipartite quantum states in a phase qubit, it is necessary to determine the parameters of the phase qubit and decoherence time. In this chapter, the procedures used to calibrate qubit parameters and decoherence time will be demonstrated. The sample is the Al phase qubit NG09Q2 and all the measurements were performed at about 20 mK. The complete calibration involves several different measurements. In the following, the readout of qubit state will be discussed first.

3.1 Readout of qubit state

To perform the readout of the qubit state, a readout pulse is used to correlate the excitation probability to the probability of tunneling to the lower potential well. The readout scheme is demonstrated in Fig. 3.1. Suppose the ground and the first excited states in the left (higher) potential well are utilized as qubit states. After a single-qubit gate operation, a short readout pulse in flux bias is applied to tilt the potential and make the left well shallower, which allows a significant probability of tunneling to the right (lower) potential well when the qubit was in the excited state. If the qubit was in the ground state, the tunneling probability is about two orders of magnitude smaller and thus the qubit will largely remain in the left well after the readout pulse is applied. Following the readout pulse, the double-well potential will be tilted back to be symmetric. Consequently, the measurement of the tunneling probability would yield the occupation probability of the excited state, *i.e.*, the excitation probability. Furthermore, the localization of the qubit state in the left or right potential well is

characterized by a circulating current in the qubit loop in the clockwise or counter-clockwise direction. Hence, by measuring the circulating current using a magnetometer, one can determine whether the tunneling happened. The magnetometer used in our experiment is an asymmetric 3-JJ dc SQUID, where a small JJ is in parallel with two larger ones connected in series, forming the two inductive arms of the SQUID. The critical currents of the junctions were chosen so that the Josephson inductance of the small junction equals to the sum of those of the two larger junctions. The benefit of the small 3-JJ dc SQUID is that it requires virtually no external flux bias to make it operate as a magnetometer.

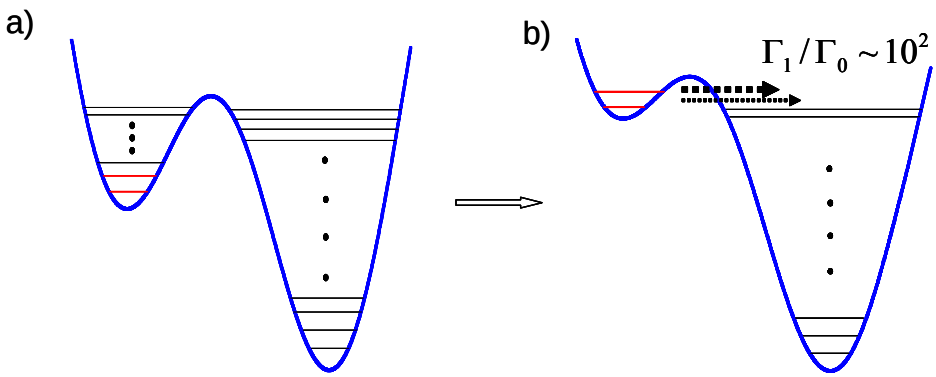

Fig. 3.1. Readout scheme of the rf SQUID phase qubit. (a) The lowest two levels localized in the higher well are used as qubit levels (marked in red). (b) A short readout pulse (~ 5 ns) is applied to tilt the potential and make the higher well shallower to allow the tunneling of the qubit in the excited state to the lower well. Γ_1 and Γ_0 are the tunneling rates when the qubit was in the excited and ground states, respectively.

Experimentally, what we measured directly is the tunneling probability of the qubit P_t, which can be converted to the excitation probability P_1 as described below.

To calibrate the relation between P_t and P_1, we used a 5-ns readout pulse and measured P_t as a function of the pulse amplitude with the qubit initialized in the ground state and the excited state, respectively. The result is shown in Fig. 3.2. When the readout pulse amplitude was increased, the higher potential well became shallower, resulting in higher rate of tunneling to the lower well. At the optimum pulse amplitude, the difference between the tunneling probabilities of qubit initialized in the ground and excited states $P_{t1} - P_{t0}$ reached its maximum value of about 0.5, giving the best contrast of the readout signal. Given the measured signal contrast, one can extract the excitation probability from the measured tunneling probability by using

$$P_1 = \frac{P_t - P_{t0}}{P_{t1} - P_{t0}}. \tag{3.1}$$

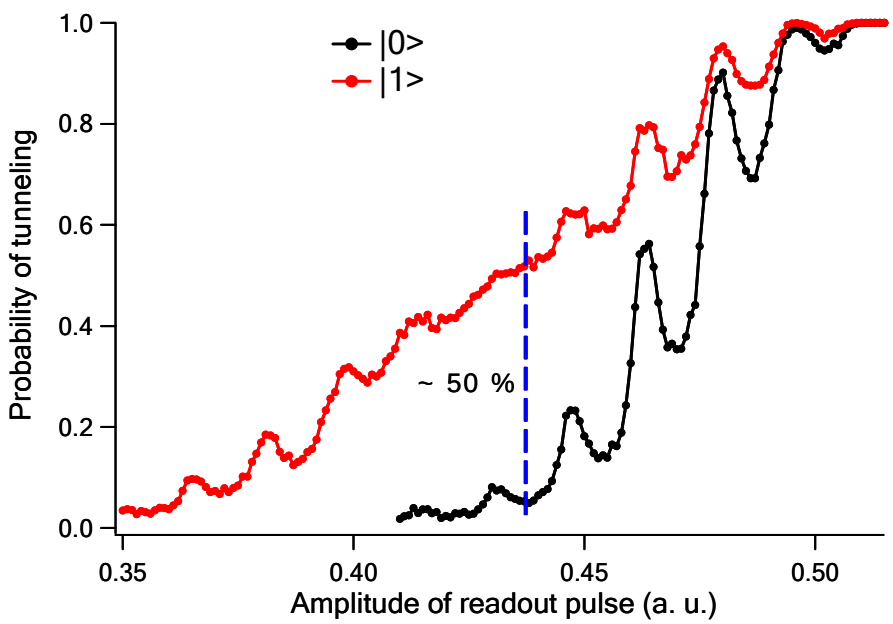

Fig. 3.2. Measured tunneling probability vs. readout pulse amplitude with qubit initialized in ground state (black curve) or excited state (red curve). The blue dashed line indicates the optimum readout amplitude and signal contrast of ~ 0.5.

The loss in the tunneling probability of the qubit initialized in the excited state

was caused by the dumping of qubit's energy to spurious two-level systems (TLSs) when the readout pulse was applied [57]. While the readout pulse changed the external flux bias to make the higher potential well shallower, the qubit's excited state was swept through avoided level crossings, where the qubit was coupled to the TLSs and was subject to the loss of the population in the excited state. Hence, the signal contrast can be significantly increased by reducing the density of TLS.

3.2 Determining the phase qubit's parameters

Three independent parameters are required to build the Hamiltonian of an isolated rf SQUID qubit: the junction's critical current I_c, the junction capacitance C, and the SQUID loop inductance L. More conveniently, one can use another set of three independent parameters: β_L, L, and C, where $\beta_L = 2\pi L I_c / \Phi_0$. In this section, we will show how to extract these qubit parameters from the spectroscopy and MRT measurements.

The phase qubit used in our experiment was operated in the gate model with microwave excitation. Hence, it is efficient to utilize the measured spectroscopy, *i.e.*, the transition frequency $\omega_{10}/2\pi$ vs. the external flux bias Φ_x, to extract the qubit's parameters. Consider the double-well potential of a phase qubit at $\Phi_x > 0.5\,\Phi_0$, where the left well is the higher well and is so deep that the barrier height $\Delta U >> \hbar\omega_{10}$. Thus the potential around the bottom of the well is approximately harmonic and thus the small oscillation frequency around the well's bottom $\omega_p \approx \omega_{10}$. Using the potential $U(\Phi)$ given in Eq. (1.22) and denoting Φ_b as the position of the left well's bottom, we have

$$\omega_p = \left(C^{-1} \frac{d^2 U}{d\Phi^2}\bigg|_{\Phi=\Phi_b} \right)^{1/2} = \sqrt{\frac{1+\beta_L \cos(2\pi\phi_b)}{LC}}, \tag{3.2}$$

where $\phi_b \equiv \Phi_b / \Phi_0$. Also note that ϕ_b satisfies the equation

$$\phi_b - \phi_x + \frac{\beta_L}{2\pi} \sin(2\pi\phi_b) = 0 \tag{3.3}$$

where $\phi_x \equiv \Phi_x / \Phi_0$. Consequently, based on Eqs. (3.2) and (3.3), any two data points (ϕ_x, ω_{10}) on the spectroscopy can be used to set up four equations to solve for ϕ_b at the two data points, β_L, and LC.

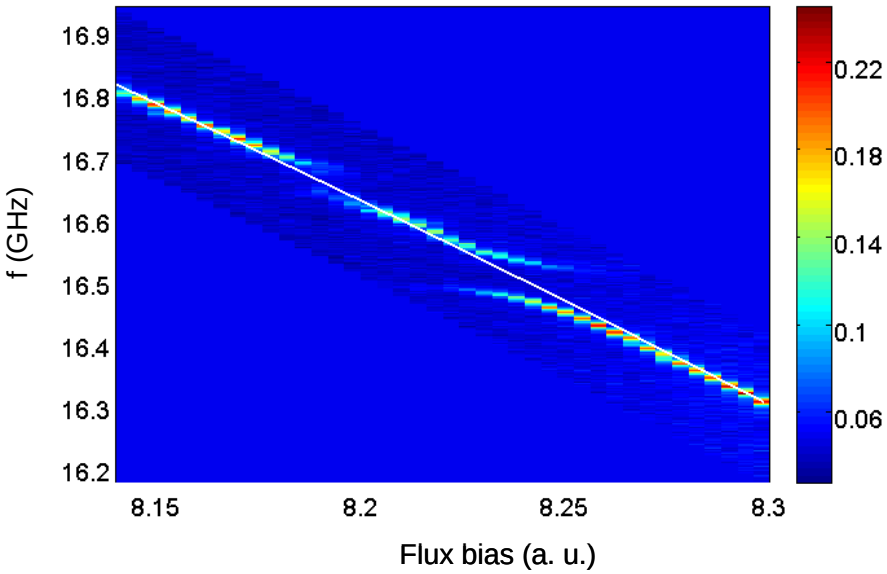

Fig. 3.3. Measured spectroscopy of the phase qubit at 20 mK and the calculated one (white curve) with $\beta_L = 3.23$ and $LC = 1.88 \times 10^5$ pH·fF.

Fig. 3.3 shows the measured spectroscopy of the phase qubit. Two obvious splittings, also called avoided crossings, in the measured spectroscopy resulted from the coupling between the qubit and spurious two level systems (TLSs). By choosing two data points away from the avoided crossings, we obtained $\beta_L = 3.23$ and $LC = 1.88 \times 10^5$ pH·fF by solving the equations described by Eqs. (3.2) and (3.3).

The relative deviation in the solved parameters was on the order of 0.1% when different data points on the spectroscopy were chosen. The numerically calculated spectroscopy based on the solved parameters was also plotted in Fig. 3.3. It went through the center of each splitting as expected and excellently matched the measured one in the region away from the splittings. The detail of the spectroscopy measurement will be given later in this chapter.

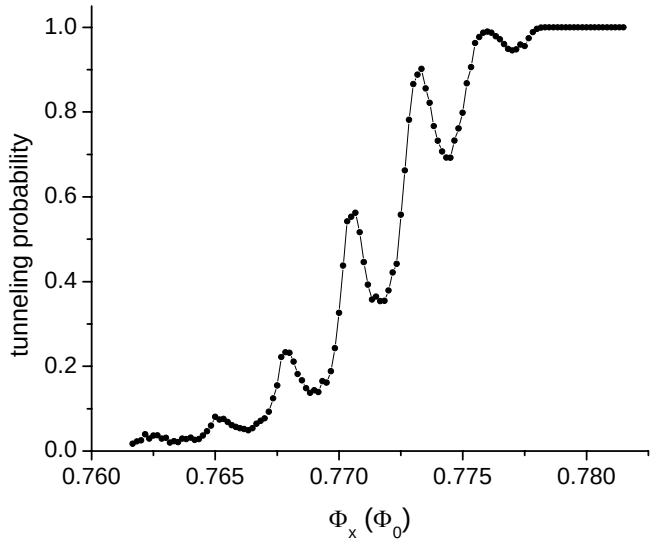

Fig. 3.4. Tunneling probability of phase qubit without microwave excitation vs. external flux bias at T = 20 mK. Peaks due to resonant tunneling are clearly seen.

In order to determine *L* and *C*, we performed the measurement of the macroscopic quantum tunneling (MRT), from which the value of *L*/*C* can be extracted. MRT occurs when the energy level of the ground state in one well is aligned with that of the state localized in the other well [22, 58]. Hence, when the tunneling probability is measured as a function of external flux bias, the maximum enhancement of tunneling probability due to MRT, called MRT peak, occurs at the flux biases where the energy levels in

opposite wells are aligned. The details of MRT measurement can be found in Refs. [59-61]. Theoretically, the flux bias interval between two adjacent MRT peaks around $\Phi_x = \Phi_0 / 2$ is given by

$$\Delta\Phi_{x\_MRT} = \frac{h}{2\Phi_0}\sqrt{L/C}\,\mathrm{f}\left(\beta_L\right), \tag{3.4}$$

where h is the Planck's constant, the function $\mathrm{f}\left(\beta_L\right) = \mathrm{f}\left(\varphi_m\right) = \sqrt{1-\varphi_m/\tan\varphi_m}/\varphi_m$, and $\beta_L = \varphi_m / \sin\varphi_m$. The derivation of Eq. (3.4) is given in Appendix D. Note that $\mathrm{f}\left(\beta_L\right)$ depends weakly on β_L. Thus the spacing between adjacent MRT peaks $\Delta\Phi_{x\_MRT}$ depends mainly on $Z_0 = \sqrt{L/C}$.

The measured tunneling probability of qubit to the right well without microwave excitation vs. flux bias is shown in Fig. 3.4, where obvious MRT peaks were observed. The spacing between adjacent MRT peaks is equal to 2.7 ± 0.1 mΦ_0 around $\Phi_x = 0.77\ \Phi_0$. Because the tunneling probability was not measured in the vicinity of $\Phi_x = \Phi_0 / 2$, we couldn't use Eq. (3.4) directly to determine L/C. Therefore, we numerically calculated the energy diagram with L/C as an adjustable parameter to fit the experimental result. Consequently, by combining the results from spectroscopy and MRT measurements, we obtained $L \approx 770$ pH and $C \approx 240$ fF.

3.3 Characterizing decoherence in the phase qubit

The measurement of coherence in time domain is required to characterize decoherence in the phase qubit. Hence, in this section, we will first demonstrate the measurement of spectroscopy and Rabi oscillations. Then we will show how to extract decoherence times from pump-probe, Ramsey fringes, and spin echo experiments.

3.3.1 Spectroscopy measurement

In order to excite the qubit with microwave, one has to measure the transition frequency $f_0 \equiv \Delta E_{10} / h$, where ΔE_{10} is the energy level spacing of the qubit states. As ΔE_{10} depends on the external flux bias Φ_x, it is measured as a function of Φ_x. At each fixed flux bias, the qubit is excited by a continuous microwave and the excitation probability P_1 is measured as a function of microwave frequency. The transition or resonant frequency is determined from the position of the maximum P_1. A measured spectroscopy is shown in Fig. 3.5. Two large splittings in the figure resulted from qubit-TLS coupling. Therefore, to study single phase qubit, we chose the flux bias at $\Phi_x = 0.679\ \Phi_0$ where the qubit was not coupled to TLS.

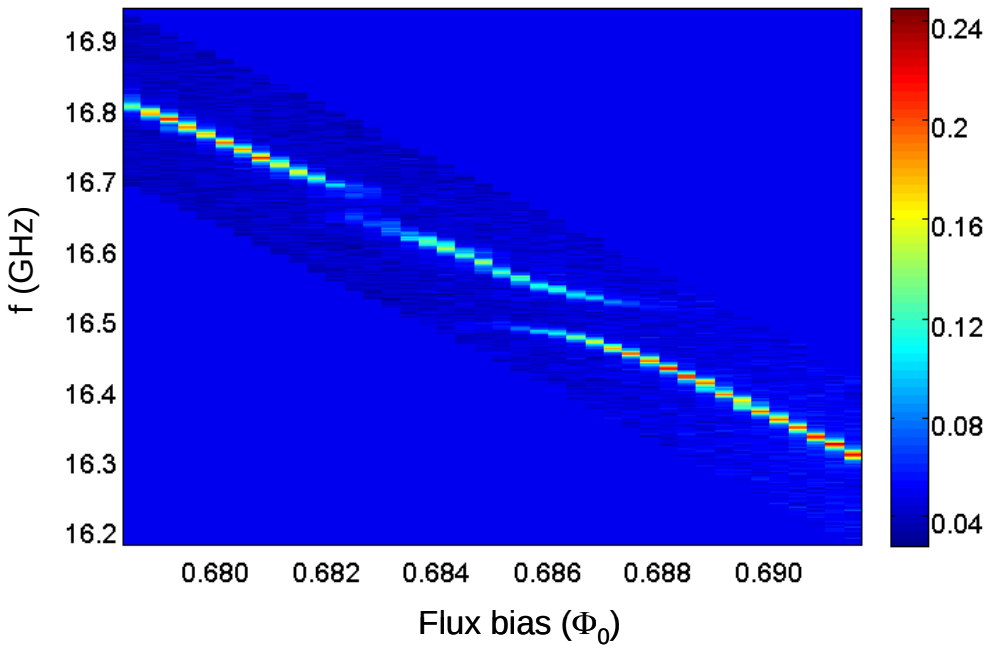

Fig. 3.5. Measured spectroscopy of the phase qubit at 20 mK, where the tunneling probability was plotted as a function of microwave frequency and flux bias. Two splittings on the spectroscopy were caused by the coupling between the qubit and two TLSs.

The measured tunneling probability vs. the frequency of applied continuous

microwave at $\Phi_x = 0.679\ \Phi_0$ is given in Fig. 3.6. The resonant peak was well fitted to a Gaussian function, yielding $f_0 = 16.777$ GHz and a Gaussian line width of 3.4 ± 0.2 MHz corresponding to a full width at half maximum (FWHM) of 8.0 MHz. Note that low power (-35 dBm) microwave and a 10 dB attenuator installed at room temperature were used to minimize the power broadening of the resonant peak. Thus the measured tunneling probability was only up to 0.12. Note that the background signal of about 0.04 was due to the finite tunneling probability of the ground state.

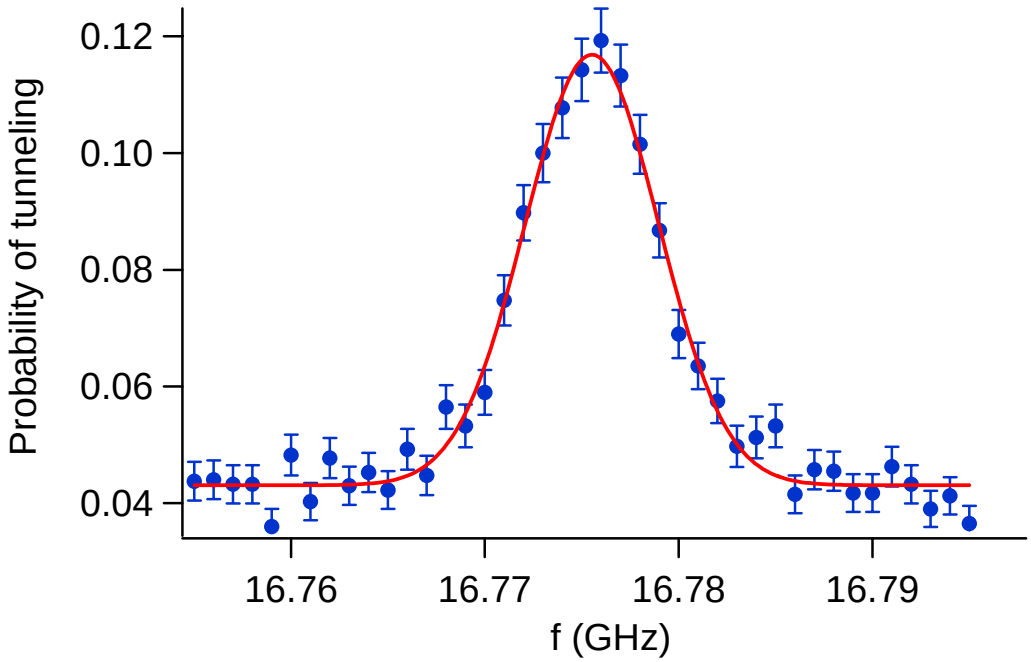

Fig. 3.6. Measured spectrum (blue dots) at $\Phi_x = 0.679\ \Phi_0$ with -35 dBm microwave power and 10 dB attenuation. The data (solid circles) with error bars was fitted to a Gaussian function (red curve).

It is well known that the homogeneous line shape for an absorptive transition is Lorentzian and under low power microwave radiation the Lorentzian line shape is

given by $L(\Delta f)=\frac{1}{\pi}\frac{1/2T_1}{\left(2\pi\Delta f\right)^2+\left(1/2T_1\right)^2}$, where Δf is the frequency detuning and T_1 is the energy relaxation time [62]. However, in the presence of Gaussian noise with amplitude distribution $G(x;\sigma)=\frac{1}{\sqrt{2\pi\sigma^2}}\exp\left(-\frac{x^2}{2\sigma^2}\right)$, where σ is the line width, the line shape is given by the convolution of the Gaussian and Lorentzian functions, *i.e.*, $\int_{-\infty}^{\infty}G(x;\sigma)L(\Delta f-x)dx$. Because the measured spectrum fitted well to the Gaussian function, the line width of the spectrum is dominated by Gaussian noise. The FWHM of the intrinsic Lorentzian line shape is given by $1/2\pi T_1\approx 2.2$ MHz, where $T_1=73$ ns is the energy relaxation time measured directly in the time domain. Thus the measured FWHM (8.0 MHz) is mostly due to the inhomogeneous broadening. For phase qubits, the inhomogeneous broadening is caused by the magnetic flux noise because the transition frequency f_0 is flux bias dependent.

More importantly, from the measured spectrum shown in Fig. 3.6, we were able to extract the intrinsic Gaussian line width, *i.e.*, the strength of the fluctuations in the transition frequency due to the flux noise, $\sigma\approx 2.8$ MHz [63]. From the measured spectroscopy as shown in Fig. 3.5, we found that at $\Phi_x=0.679\ \Phi_0$ the derivative $\partial f_0/\partial\Phi_x\approx 33$ MHz/mΦ_0. Thus the rms of the flux noise is about $2.8/33\approx 0.09$ mΦ_0, comparable to the values observed by other groups in Al phase qubits with similar geometry and size [49]. We will show later how to characterize the pure dephasing induced by flux noise.

3.3.2 Rabi oscillations

Quantum coherence in time domain can be demonstrated by the observation of

Rabi oscillations in qubits. To measure Rabi oscillations, a microwave pulse with varying pulse duration is applied to excite the qubit and is followed by a readout pulse immediately. When on-resonance microwave is applied, one will observe the on-resonance Rabi oscillation, where the excitation probability is given in Eq. (1.14).

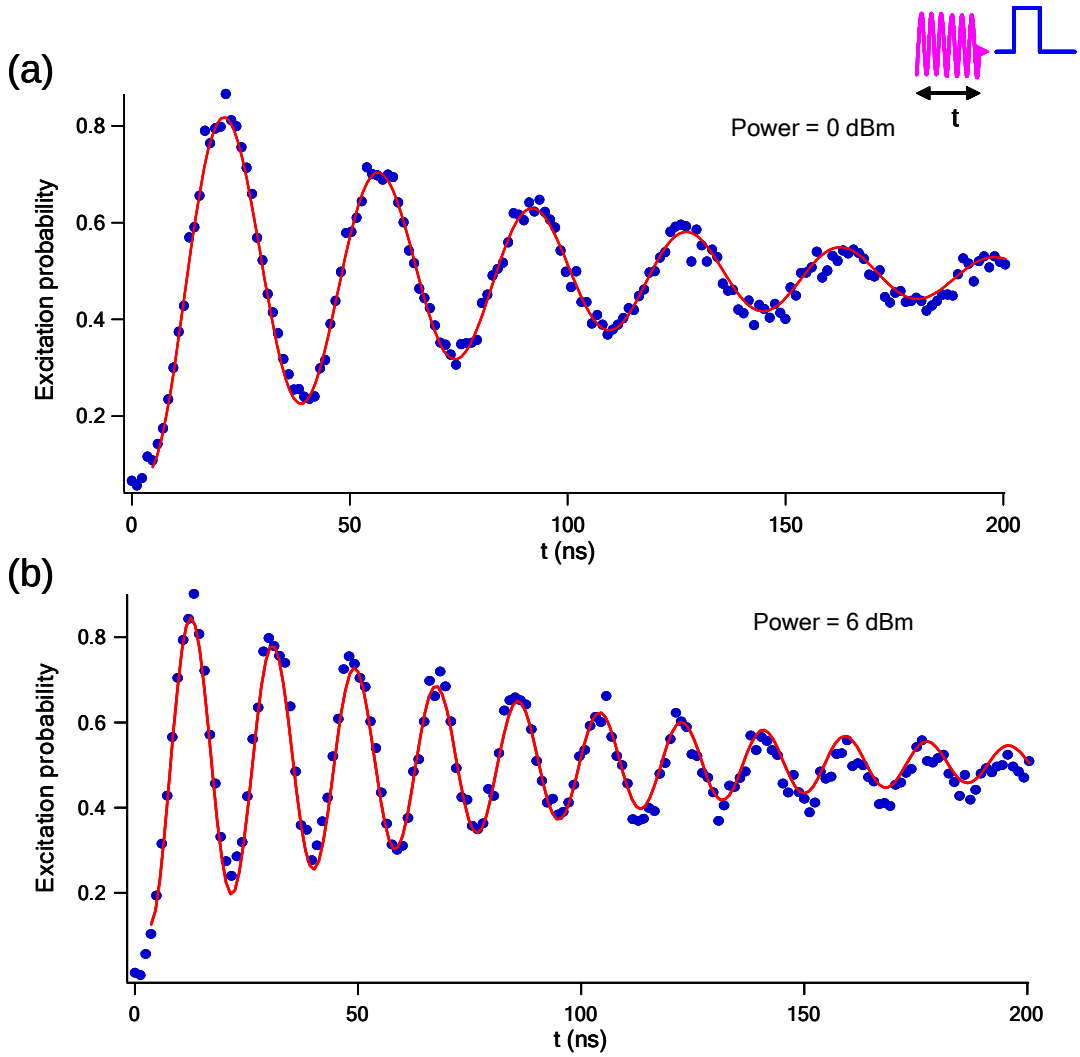

Fig. 3.7. Rabi oscillations at microwave power of 0 dBm (a) and 6 dBm (b) with the microwave frequency f = 16.777 GHz. The data was fitted to a sinusoidal function with an exponential decay amplitude (red curve). Inset: a sketch shows the timing of the microwave pulse and the readout pulse.

The flux bias was still set to $\Phi_x = 0.679\ \Phi_0$. Fig. 3.7 shows the measured Rabi oscillations at microwave frequency $f = 16.777$ GHz and microwave powers P_{mw} = 0

and 6 dBm, respectively. The measured tunneling probability was converted into excitation probability and then was fitted to a sinusoidal function whose amplitude decays exponentially with time. The best fit yields both the frequency and decay time of the Rabi oscillation. As described in Chap 1, the Rabi frequency scales with the microwave amplitude at low power microwave excitation. Note that the microwave power needs to be calibrated because two mixers and a diplexer used in the microwave line have frequency-dependent insertion losses. Fig. 3.8 shows the measured Rabi frequency vs. microwave amplitude at $\Phi_x = 0.693\,\Phi_0$. The Rabi frequency scales with the microwave amplitude linearly, as expected from the theory.

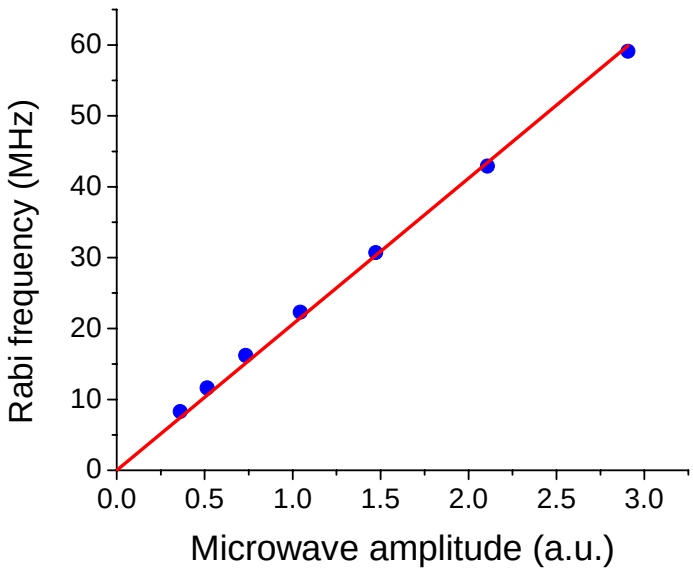

Fig. 3.8. Measured Rabi frequency vs. microwave amplitude at low power microwave excitation. The red line is the best linear fit to the data.

The Rabi decay time $T_R = 84 \pm 2$ ns was obtained from the Rabi oscillations shown in Fig. 3.7. Theoretically, T_R is related to the energy relaxation time T_1 by

$$T_R^{-1} = \left(\frac{4}{3}T_1\right)^{-1} + \left(2T_v\right)^{-1} \tag{3.5}$$

where the rate $1/T_v$ is determined by the flux noise spectral density at the Rabi frequency [64].

Fig. 3.9 shows the Rabi oscillations at f = 16.777 GHz and 16.827 GHz with fixed microwave power $P_{mw} = 9$ dBm at $\Phi_x = 0.679\ \Phi_0$. Note that 16.777 GHz is the resonant frequency extracted from the measured spectrum so that 16.827 GHz is 50 MHz detuned from the resonance. Compared to the on-resonance Rabi oscillation, the detuned Rabi oscillation at 16.827 GHz has a smaller amplitude and higher frequency. The width of the detuned π/2-pulse can be extracted from the best fit to the data and it will be used later in the Ramsey fringe experiment.

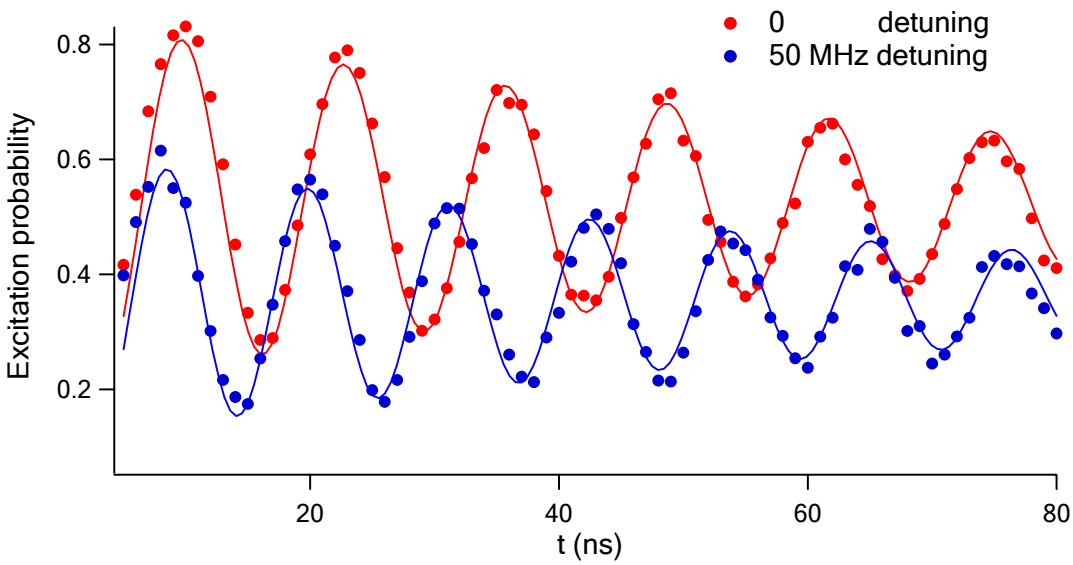

Fig. 3.9. Rabi oscillations at f = 16.777 GHz and 16.827 GHz with fixed microwave power = 9 dBm at $\Phi_x = 0.679\ \Phi_0$. Solid curves are the best fits to the data.

3.3.3 Energy relaxation time

The energy relaxation time T_1 can be obtained from the pump-probe experiment,

where the excitation probability is measured as a function of free evolution time after the qubit is prepared in the excited state by a π-pulse. Fig. 3.10 shows the result of such a measurement at $\Phi_x = 0.679\ \Phi_0$. The best fit to an exponential decay gave $T_1 = 73 \pm 1$ ns. In addition, we observed the variation in T_1 at different flux biases. When the flux bias was in the region with many small avoided crossings, T_1 was found to decrease to about 60 ns. It revealed the energy exchange between the qubit and TLSs could reduce T_1.

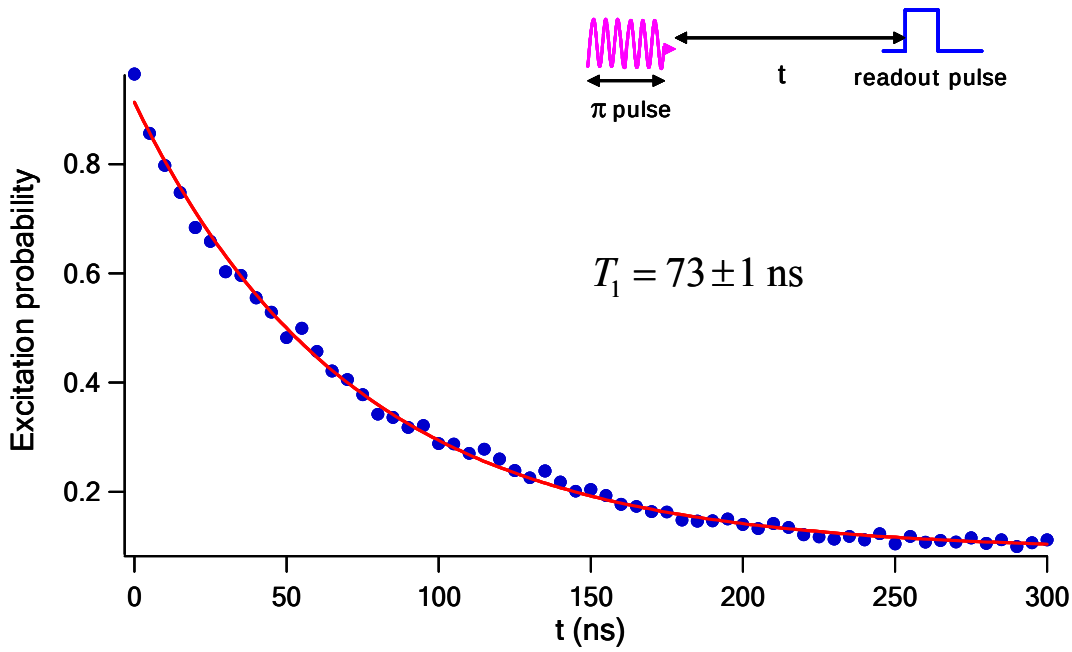

Fig. 3.10. Excitation probability as a function of the delay time between the π-pulse and the readout pulse at $\Phi_x = 0.679\ \Phi_0$. The red curve is the best exponential fit to the data.

From the measured T_1, the quality factor Q can be estimated. The homogeneous line shape of an absorptive transition is Lorentzian $\propto \frac{1}{(\Delta\omega)^2 + (1/2T_1)^2}$, where $\Delta\omega = 2\pi(f - f_0)$ and the FWHM is given by $1/T_1$. Therefore, T_1=73 ns corresponds

to $Q = \frac{\omega_0}{\text{FWHM}} = \omega_0 T_1 \approx 7500$.

3.3.4 Pure dephasing time determined from Ramsey fringes

To characterize dephasing in the phase qubit, we measured the rate of the free-induced decay using the Ramsey pulse sequence. The Ramsey pulse sequence consists of two detuned π/2-pulses separated by a period of t during which the qubit state evolves freely. The corresponding evolution of the qubit state on Bloch sphere is shown in Fig. 3.11, where a simple case of $\Delta\omega \ll \Omega_0$ is assumed for the purpose of illustration.

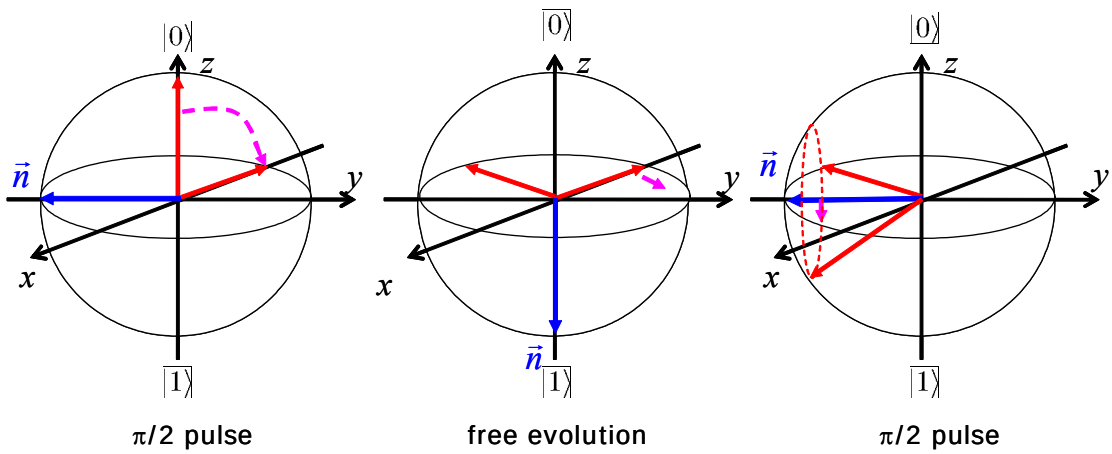

Fig. 3.11. Manipulation of qubit state for Ramsey pulse sequence is illustrated on the Bloch sphere. First, the qubit state vector (red) is brought to the x-y plane by the first π/2-pulse. Then it is allowed to evolve freely, where the state vector will rotate about -z axis by angle $\Delta\omega t$. Subsequently, the second π/2-pulse brings the vector to the y-z plane.

In the absence of decoherence, when $\Delta\omega \ll \Omega_0$ the excitation probability after the Ramsey pulse sequence is given by $P_1 = \frac{1+\cos(\Delta\omega t)}{2}$, where $\Delta\omega / 2\pi = \Delta f$ is the frequency detuning. Denote $\delta f \equiv \delta\omega / 2\pi$ as the fluctuation of the transition frequency caused by Gaussian flux noise. Thus the average of $\cos(\delta\omega t)$ is given by

$\int_{-\infty}^{\infty} G(\delta f;\sigma)\cos(\delta\omega t)\,d(\delta f) = \exp\left[-\frac{(2\pi\sigma t)^2}{2}\right]$, where $G(\delta f;\sigma)$ is a Gaussian function of δf with the line width σ. Consequently, in the presence of pure dephasing induced by flux noise, by defining $T_\varphi = \frac{\sqrt{2}}{2\pi\sigma}$, the excitation probability can be written as

$$P_1(t) = \frac{1+\cos(\Delta\omega t)\langle\cos(\delta\omega t)\rangle}{2} = \frac{1}{2}\left\{1+\cos(\Delta\omega t)\exp\left[-(t/T_\varphi)^2\right]\right\}, \qquad (3.6)$$

where $1/T_\varphi$ is the pure dephasing rate. Eq. (3.6) shows that the decay of Ramsey fringe signal due to pure dephasing is non-exponential. Note that the Gaussian decay described by Eq. (3.6) only requires the noise to be random, thus having a Gaussian distribution of amplitude. It doesn't require the noise spectral density to have a specific form, such as the $1/f$ or white noise. By also considering the effect of homogeneous dephasing, finally we have

$$P_1(t) = \frac{1}{2}\left\{1+\cos(\Delta\omega t)\exp\left[-(t/T_\varphi)^2 - t/2T_1\right]\right\}. \qquad (3.7)$$

To our knowledge, the accurate determination of T_φ in a phase qubit from Ramsey fringes hasn't been reported before. Thus, experimental confirmation of (3.7) is important to have a better understanding of the dephasing process in phase qubits. To perform the Ramsey fringe experiment accurately, we carefully calibrated the width of the detuned microwave pulse. When the detuning was 50 MHz, the width of the detuned π/2-pulse is 4.7 ns. The result of Ramsey fringe measurement is shown in Fig. 3.12, where the excitation probability was measured as a function of the duration of the free evolution at $\Phi_x = 0.679\ \Phi_0$ and was then normalized. The signal of Ramsey fringes was fitted to the function given in Eq. (3.7) with the measured $T_1 = 73 \pm 1$ ns,

yielding $T_\varphi = 81 \pm 2$ ns. Thus $\sigma = \frac{\sqrt{2}}{2\pi T_\varphi} = 2.78 \pm 0.07$ MHz, consistent with the value of the Gaussian line width (2.8 MHz) extracted from the spectrum measurement, corresponding to the rms flux noise of 84 $\mu\Phi_0$. The result shows that the pure dephasing rate can be accurately determined from the Ramsey fringe measurement.

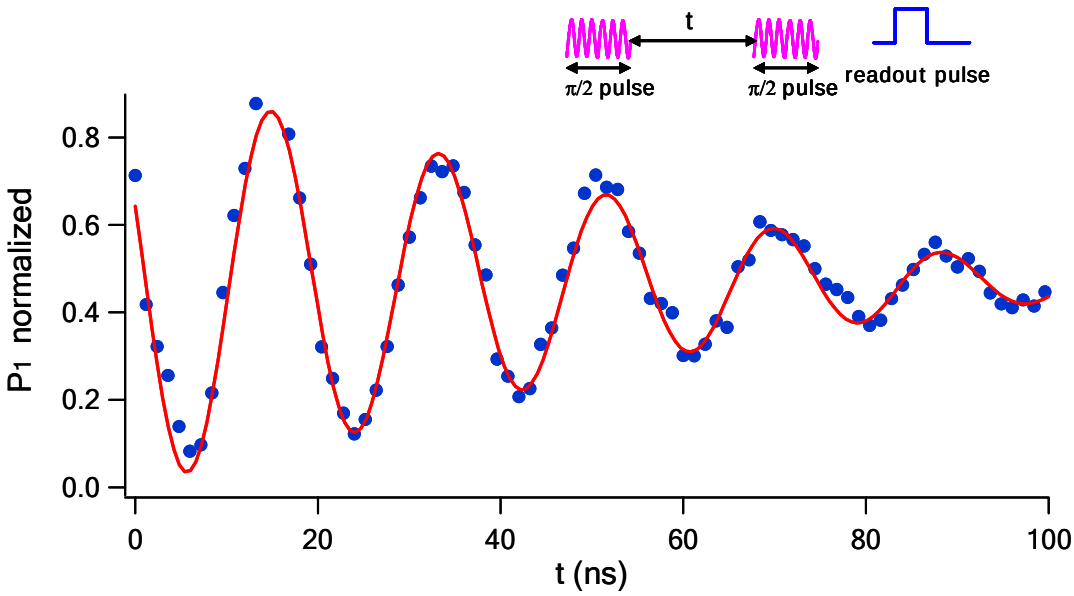

Fig. 3.12. Signal of Ramsey fringes with 50 MHz detuning. The red curve is the best fit to the function described by Eq. (3.7), where $T_1 = 73$ ns. The fit yields $T_\varphi = 81 \pm 2$ ns.

3.3.5 Decoherence time determined from spin echo experiment

In nuclear magnetic resonance (NMR), a technique called "spin echo" is used to refocus the precessing nuclear spins to eliminate the inhomogeneous dephasing caused by magnetic field gradients [65]. As discussed in Chapter 1, the transition frequency of the qubit fluctuates due to the low frequency flux noise, resulting in randomization of the precession speed of the qubit state vector. Therefore, the spin echo technique can also be used here to suppress inhomogeneous dephasing induced by the low frequency flux noise in phase qubits.

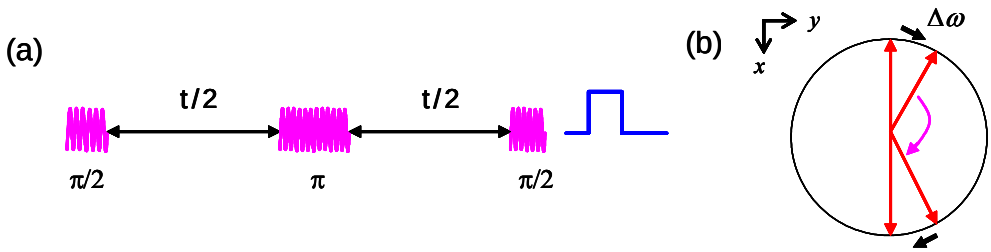

Fig. 3.13. (a) Spin echo pulse sequence followed by a readout pulse, where the total free evolution time is *t*. (b) Refocus of state vectors on the x-y plane by the π-pulse.

A conventional spin echo pulse sequence consists of three on-resonance pulses: two π/2-pulses interrupted by a refocusing π-pulse with equal time interval of free evolution between consecutive pulses as shown in Fig. 3.13. (a). The first π/2-pulse brings the state vector onto the *x*-*y* plane. Then the state vector is allowed to rotate about the -*z* axis for a period of *t*/2. Consider two qubit particles, where the state vector of one qubit particles rotates $\delta\omega$ faster than the other. Thus it would be $\delta\omega t/2$ ahead after the first period of free evolution. Then the state vector will be rotated by 180° about the -*y* axis by a π-pulse and consequently it would be $\delta\omega t/2$ behind. However, after the second *t*/2 free evolution, it will catch up the state vector of the other qubit, as shown in Fig. 3.13. (b). Hence, the states of qubit particles are "refocused" and the pure dephasing is eliminated. The second π/2-pulse takes the state vector back into the *y*-*z* plane, which is followed by the readout pulse. In the above description, $\delta\omega$ is assumed to be constant in the time scale of free evolution, typically 10 – 10^2 ns. Obviously, the spin echo pulse sequence can't suppress dephasing induced by the flux noise with frequency greater than 1/*t*, where $\delta\omega$ varies during the period of free evolution.

Fig. 3.14 shows the measured signal of spin echo as a function of the total time of free evolution t at $\Phi_x = 0.679\ \Phi_0$. Following the convention, we used $1-P_1$ as the spin echo signal. In Fig. 3.14, the data was fitted to an exponential decay, giving the time constant $T_{2E} = 138 \pm 5$ ns, which is very close to $2T_1 = 146$ ns. The result indicates that the effect of pure dephasing has been significantly reduced in the spin echo experiment.

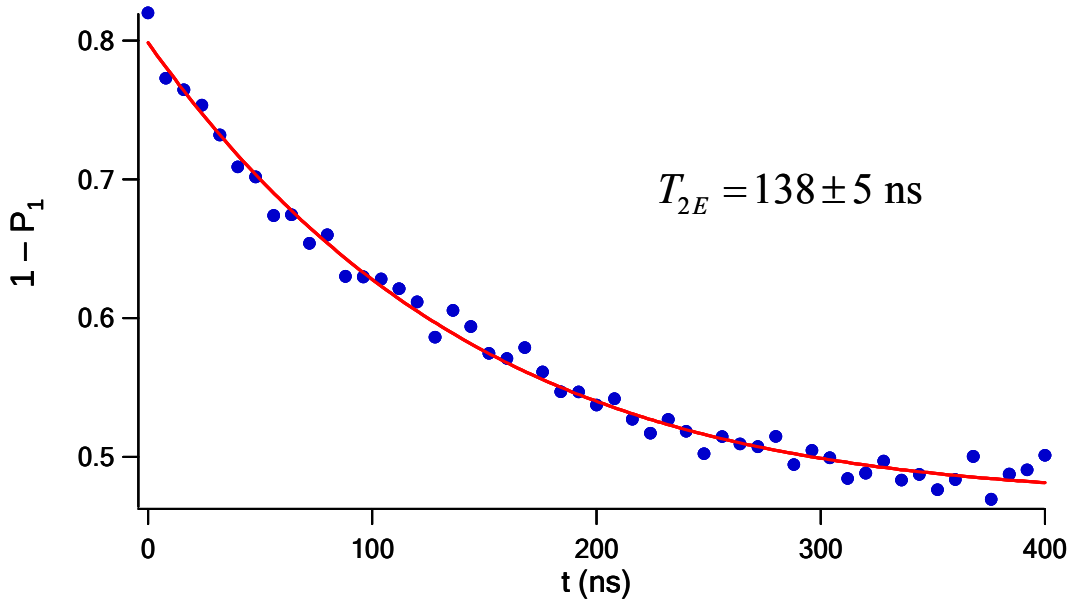

Fig. 3.14. Spin echo signal vs. the free evolution time at $\Phi_x = 0.679\ \Phi_0$. The data is fitted an exponential decay, yielding $T_{2E} = 138 \pm 5$ ns.

Furthermore, to determine the pure dephasing rate $1/T_{\varphi E}$, the spin echo signal was fitted to the function given in Eq. (3.7) with the detuning $\Delta\omega = 0$ and $T_1 = 73$ ns, as shown in Fig. 3.15. The fitting yielded $T_{\varphi E} = 500 \pm 100$ ns and the spin echo dephasing rate $1/T_{\varphi E} \approx 2\times10^6$ s^{-1}, which is about 6 times smaller than the dephasing rate extracted from the Ramsey fringe experiment.

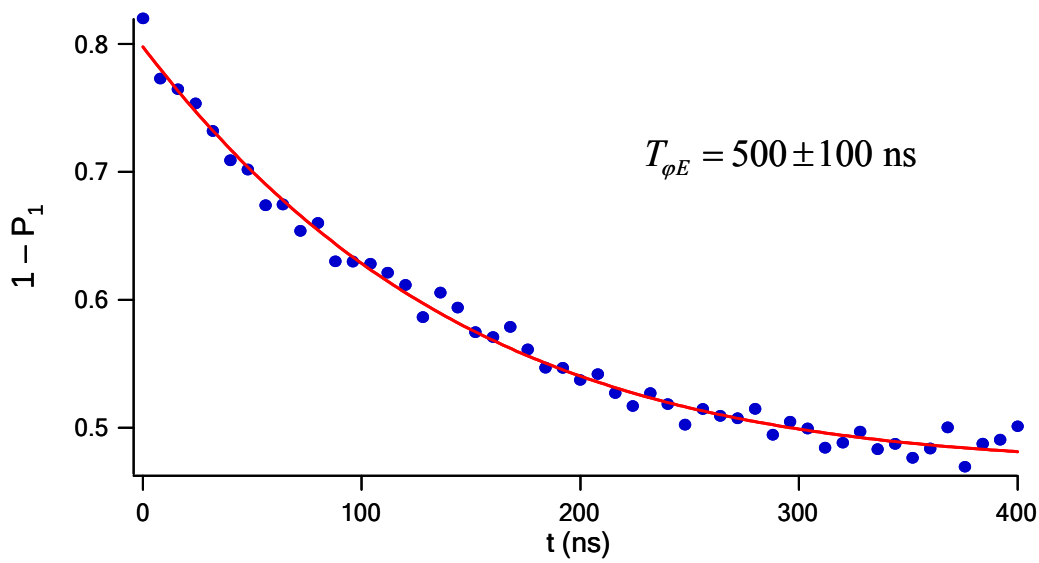

Fig. 3.15. Signal of spin echo fitted to the function given in Eq. (3.7) with $\Delta\omega = 0$ and $T_1 = 73$ ns. The fit yields $T_{\varphi E} = 500 \pm 100$ ns.

Similar work on decoherence characterization has been done in Al 3-JJ flux qubits [47], which had an optimum bias point where the transition frequency is virtually independent of small flux noise. A spin echo decoherence time $T_{2E} \approx 2T_1$ was reported only in the vicinity of the optimum bias point. In other bias regions, the qubit was subject to pure dephasing induced by flux noise and significantly greater pure dephasing rate in spin echo experiments was observed. It indicated that there was substantial high frequency flux noise in 3-JJ flux qubits, where the resulting dephasing couldn't be suppressed by the conventional spin echo pulse sequence. Thus, it is interesting to investigate whether there is also significant high frequency flux noise in phase qubits. Dephasing induced by high frequency noise can be suppressed by dynamical decoupling (DD) pulse sequences [66]. For example, the coherence time of electron spins in malonic acid crystals was improved from 6 μs with conventional spin

echo sequence to about 30 μs by using a DD pulse sequence to decouple the qubits from the high frequency noise [66, 67]. At a different flux bias, we tried the second order DD pulse sequence, where the single π-pulse in the conventional spin echo sequence was replaced by double π-pulses. However, the measured dephasing rate was essentially the same as before, indicating that the pure dephasing induced by high frequency (>10 MHz) flux noise in our phase qubit is negligible.

Chapter 4. Coherent manipulation of multi-partite quantum states by LZ transitions

In this chapter, we will demonstrate the coherent manipulation of multi-partite quantum states via LZ transitions in the phase qubit coupled to two TLSs. In addition, it will be shown that the multi-qubit gates using LZ transitions have much shorter gate time and are easier to be implemented, compared to the conventional quantum gates controlled by microwave pulses. The measurement of spontaneous coherent oscillations in a coupled qubit-TLS bipartite system will be discussed first, which yields the qubit-TLS coupling strength. Next, the experimental result of Landau-Zener-Stückelberg (LZS) interference in a tripartite system will be shown and compared to the theoretical calculations based on the independently calibrated parameters of the phase qubit. Finally, we will discuss how to create the W state in the tripartite system by utilizing LZ transitions.

4.1 Phase qubit coupled to TLSs

As mentioned in Chapter 3, at certain flux biases, the phase qubit was strongly coupled to spurious TLSs, resulting in avoided level crossings in the spectroscopy. In general, TLSs are found in amorphous materials due to the random bonding of atoms [68]. For superconducting phase qubits, TLSs come from the oxide barrier of the tunnel junction and the density of TLS can be reduced by using small-area junctions [33, 69]. On the other hand, a qubit coupled to TLSs is also an excellent multi-partite quantum system, which can be utilized as a prototypical multi-qubit system to study

various interesting quantum phenomena, such as entanglement [32, 70].

Consider the simplest case where the qubit is coupled to one TLS. Denote $\hbar\omega_{10}$ as the energy level spacing between the qubit states $|0\rangle$ and $|1\rangle$, and $\hbar\omega_{TLS}$ as the energy level spacing between the ground state $|g\rangle$ and excited state $|e\rangle$ of the TLS. When ω_{10} is close to ω_{TLS}, coupling between the qubit and TLS becomes strong and leads to avoided level crossing. Note that ω_{TLS} is independent of flux bias while ω_0 is flux bias dependent. The basis states for the coupled qubit-TLS system are $|0g\rangle$, $|1g\rangle$, $|0e\rangle$, and $|1e\rangle$. At the degeneracy point where $|0e\rangle$ and $|1g\rangle$ have the same energy, the ground and excited states of the coupled qubit-TLS system are given by $\left(|1g\rangle+|0e\rangle\right)/\sqrt{2}$ and $\left(|1g\rangle-|0e\rangle\right)/\sqrt{2}$, respectively. The tunnel splitting Δ is defined as the energy difference between the eigenstates at the degeneracy point.

To realize spontaneous coherent oscillations between $|1g\rangle$ and $|0e\rangle$, we used a microwave pulse to excite the qubit from $|0g\rangle$ to $|1g\rangle$. Then the system was allowed to evolve freely, as shown in the inset of Fig. 4.1. In general, the coupled qubit-TLS is a four-level system. However, $|1g\rangle$ and $|0e\rangle$ are the only two effective basis states needed to study the dynamics during the free evolution. The effective Hamiltonian is thus given by

$$\hat{H}=\begin{pmatrix}\hbar\omega_{10} & -\Delta/2\\ -\Delta/2 & \hbar\omega_{TLS}\end{pmatrix}, \tag{4.1}$$

where $\Delta/2$ is the coupling strength between $|1g\rangle$ and $|0e\rangle$. By defining the energy difference $\varepsilon=\hbar\omega_{TLS}-\hbar\omega_{10}$, the effective Hamiltonian can be written as $\hat{H}=-\frac{1}{2}\left(\varepsilon\sigma_z+\Delta\sigma_x\right)$, the same form as the Hamiltonian of a flux qubit. From Eq. (4.1), it is straightforward to show that the spontaneous coherent oscillation between $|1g\rangle$

and $|0e\rangle$ occurs during the free evolution, where the oscillation frequency $f_s = \sqrt{\Delta^2 + \varepsilon^2}/h$. Thus at the degeneracy point where $\varepsilon = 0$, the oscillation frequency is simply given by Δ/h. Note that the spontaneous coherent oscillation shown here is similar to the vacuum Rabi oscillation in an excited atom coupled to a resonator or cavity [71].

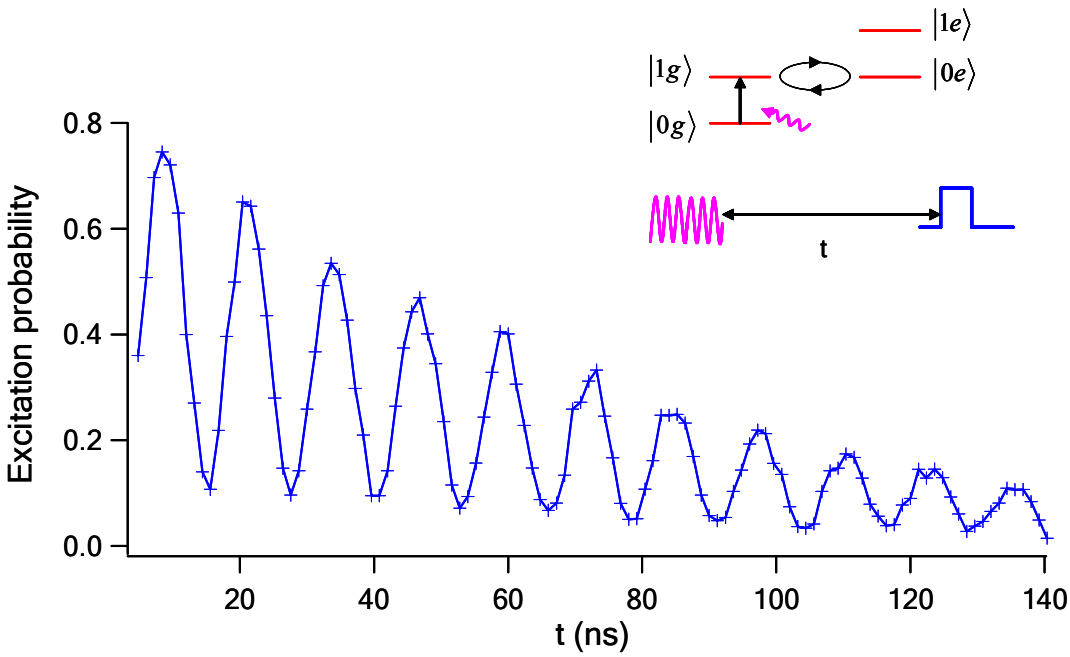

Fig. 4.1. Observed coherent oscillation between $|1g\rangle$ and $|0e\rangle$ in the phase qubit coupled to single TLS, where the data points (crosses) are connected by straight lines for eye guidance. Inset shows the energy levels and pulse sequence.

A typical coherent oscillation in the qubit-TLS system is illustrated in Fig. 4.1, where the measured occupation probability of $|1g\rangle$ and $|1e\rangle$ at the degeneracy point is plotted as a function of the free evolution time. Note that the decreasing amplitude of the oscillation was due to the relaxation from $|1g\rangle$ to $|0g\rangle$ and $|0e\rangle$ to $|0g\rangle$. More importantly, one can accurately determine the oscillation frequency by fitting the

measured spontaneous oscillations and thus obtain the coupling strength between the qubit and TLS.

4.2 Landau-Zener transition

A qubit prepared in the ground state could be taken into the excited state by LZ transition when the system is quickly manipulated through the avoided level crossing between the qubit states. The LZ transition probability is given by

$$P_{LZ} = \exp\left(\frac{-\pi\Delta^2}{2\hbar v}\right), \tag{4.2}$$

where $v = dE/dt$ is the sweeping rate of energy and Δ is the tunnel splitting. Hence, when the sweeping is fast enough to make $\Delta^2/\hbar v \leq 1$, the transition is a diabatic process where a significant part of the qubit's wavefunction would be coherently transferred to the excited state. Hence, the avoided crossings function as a beam splitter due to the significant transition probability. Hereafter, the system will evolve adiabatically.

Fig. 4.2 shows a LZ transition at one avoided crossing in a coupled qubit-TLS system. The system is prepared in state $|1g\rangle$ by a π-pulse and then the flux bias is swept through the avoided crossing. If the sweep rate is small, the process is adiabatic and the system will remain in the higher level state. However, if the sweep rate is sufficiently high, the system will have a significant probability of making a transition to the lower level state, *i.e.*, taking the path indicated by the blue arrow. In this case, the wavefunction after the LZ transition is given by

$$|\psi\rangle = \sqrt{1-P_{LZ}}\,|0e\rangle - e^{-i\tilde{\varphi}_s}\sqrt{P_{LZ}}\,|1g\rangle, \tag{4.3}$$

where the phase jump $\tilde{\varphi}_s$ is related to the so-called Stokes phase φ_s by $\tilde{\varphi}_s = \varphi_s - \frac{\pi}{2}$ [72]. The Stokes phase is given by

$$\varphi_s = \frac{\pi}{4} + \delta(\ln\delta - 1) + \arg\left[\Gamma(1 - i\delta)\right], \qquad (4.4)$$

where $\delta = \frac{\Delta^2}{4\hbar v}$ and Γ is the gamma function. Note that φ_s is a monotonous function of δ with $\varphi_s = 0$ in the adiabatic limit ($\delta >> 1$) and $\varphi_s = \frac{\pi}{4}$ in the diabatic limit ($\delta << 1$). Eq. (4.3) shows that the avoided crossing acts as an adjustable beam splitter for the system's wavefunction.

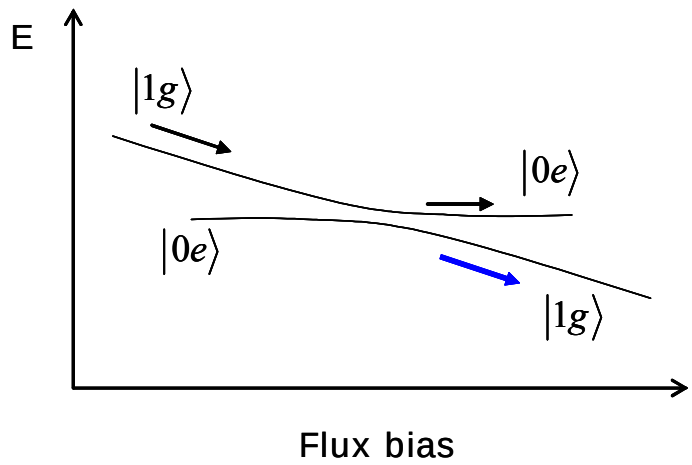

Fig. 4.2. Schematic drawing of LZ transition in a qubit-TLS system. The system is swept through the crossing between $|1g\rangle$ and $|0e\rangle$ after initialized in state $|1g\rangle$. With a high sweeping rate, the probability of LZ transition (taking the path indicated by the blue arrow) becomes significant.

4.3 Landau-Zener-Stückelberg (LZS) interference in a tripartite system

Interesting quantum interference may occur when one sweeps the flux bias forth and back through a single avoided crossing, where two LZ transitions occur. Between the two LZ transitions, the system will evolve adiabatically. After the second LZ

transition, the probability of finding the system in state $|1g\rangle$ is given by $\left|C_0 + C_1 e^{-i\varphi}\right|^2$, where C_0 and C_1 are real numbers related to P_{LZ}, and φ is the phase difference accumulated in the adiabatic evolution and LZ transitions. Consequently, the so-called Landau-Zener-Stückelberg (LZS) quantum interference can be observed and the extrema of the probability occur at $\varphi = 2N\pi$, where N is an integer [72].

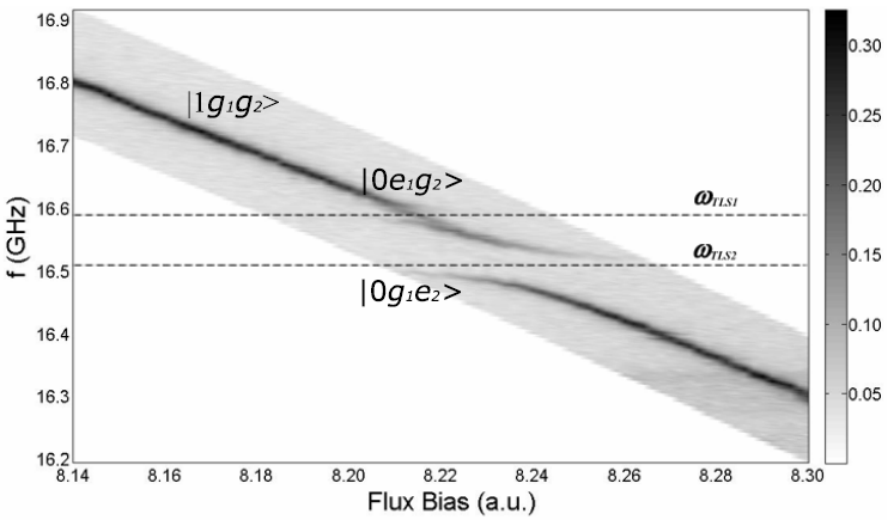

Fig. 4.3. Two avoided level crossings due to coupling to two TLSs in the measured spectroscopy. The first tunnel splitting is much smaller than the second one, *i.e.*, $\Delta_1 < \Delta_2$. $\omega_{TLS1}/2\pi$ and $\omega_{TLS2}/2\pi$ are the transition frequencies of the two TLSs, respectively.

Moreover, when one sweeps the flux bias through more than one avoided crossings, more interesting phenomenon of quantum interference is expected. As shown in the measured spectroscopy of Fig. 4.3, there were two avoided crossings, due to the coupling of qubit to two TLSs. In addition, $\Delta_1 = 20$ MHz and $\Delta_2 = 64$ MHz, indicating the coupling to the second TLS was much stronger than that to the first one. Hence, the qubit and two TLSs formed a coupled tripartite quantum system and only

three excited states $|1g_1g_2\rangle$, $|0e_1g_2\rangle$, and $|0g_1e_2\rangle$ were involved, as indicated in Fig. 4.3. This is strictly true in the absence of energy relaxation since the total energy of the system is conserved. With finite dissipation, the system has a finite probability of decaying to the ground state. In the following discussion, we denote the transition frequencies for the two TLSs as $\omega_{TLS1}/2\pi$ and $\omega_{TLS2}/2\pi$, respectively.

Based on the measured spectroscopy, we found that for a tunnel splitting of 20 MHz, the sweeping rate of flux bias is required to be greater than 0.1 $\mathrm{m}\Phi_0/\mathrm{ns}$ to have significant LZ transition probability. In addition, the operation time for coherent manipulation is limited by the measured decoherence time ~ 100 ns. Thus controlling the flux bias via the readout pulse line turned out to be the best way because the readout pulse line has a cutoff frequency of up to several GHz and is adequately coupled to the phase qubit. Consequently, by applying an isosceles triangle pulse with varying pulse duration to sweep the flux bias, we were able to observe the LZS interference pattern. Furthermore, by varying the amplitude of the triangle pulse, we measured the two dimensional LZS interference pattern [73]. Note that the isosceles triangle pulse was used to keep the sweeping rate v fixed during the flux bias sweeping. The time resolution of the triangle pulse is 0.1 ns, sufficient for the precise control of the flux bias.

In the experiment, the system was prepared in $|1g_1g_2\rangle$ from the ground state $|0g_1g_2\rangle$ by a π-pulse. Then the microwave was turned off and the state of this tripartite quantum system was manipulated only by the isosceles triangle pulse applied to the flux bias. The dc flux bias was set away from the two avoided crossings, as

shown in Fig. 4.4 (d). The pulse amplitude was varied from zero to the value which is sufficiently large to make the total flux bias pass the second avoided crossing (labeled as "M_2"). Different energy sweeping rates were obtained with different combinations of the pulse duration and pulse amplitude. Fig. 4.4 (a) shows the measured occupation probability of $|1g_1g_2\rangle$ as a function of the pulse duration and amplitude.

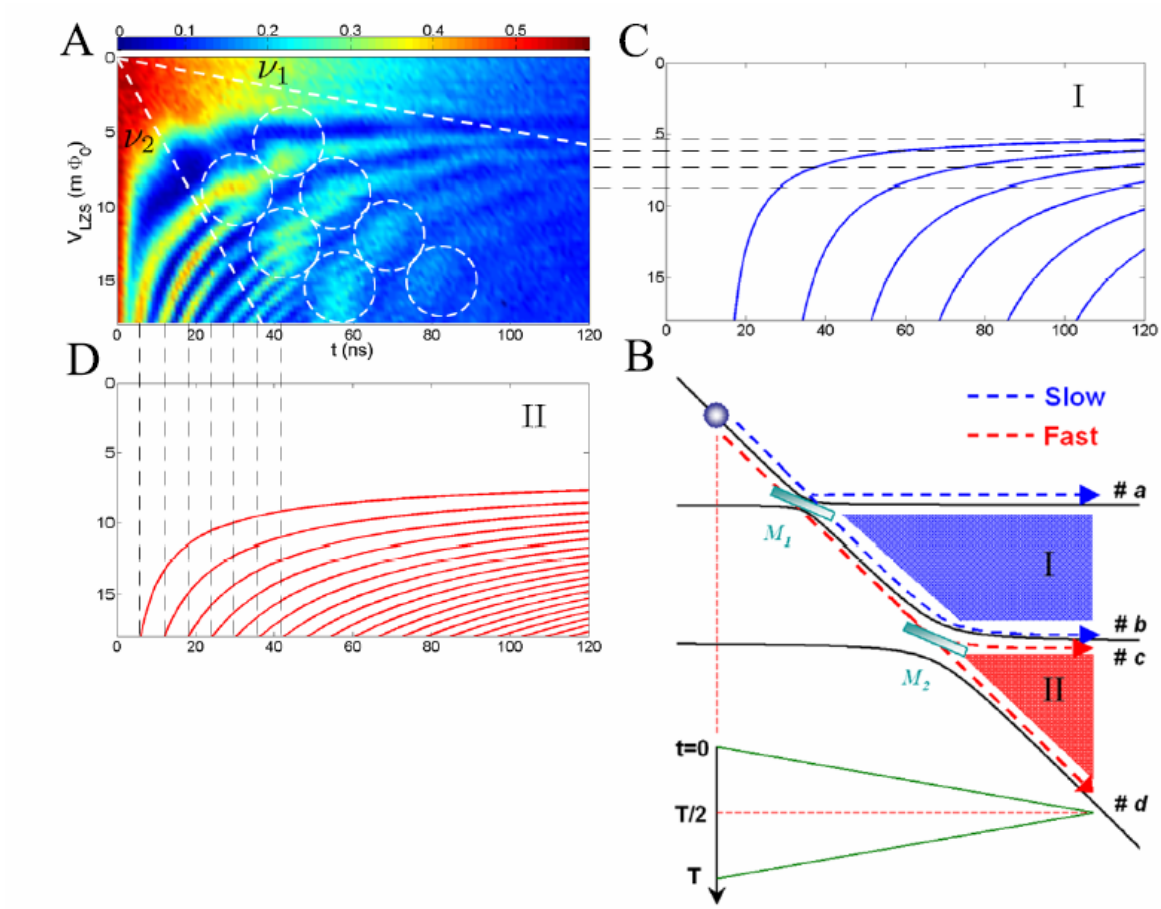

Fig. 4.4. (a) Measured occupation probability of $|1g_1g_2\rangle$ vs. the amplitude and duration of the triangle pulse. (b) and (c) Predicted positions of constructive interference in region I and II, respectively. (d) Schematic drawing of the two avoided crossings operating as beam splitters and the triangle pulse of the flux bias.

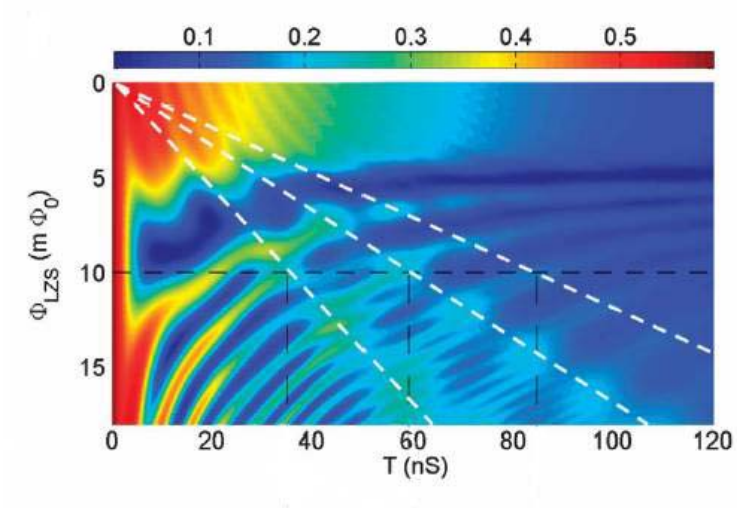

Fig. 4.5. Numerically simulated LZS interference pattern base on the experimentally calibrated system parameters. The picture is modified from Ref. [73].

Define two characteristic sweeping rates v_1 and v_2 given by $\pi\Delta_i^{\ 2}/2\hbar v_i = 1,\ i = 1,2,$ and note that $\Delta_1 < \Delta_2$ as shown in the measured spectroscopy. One can analytically investigate the interference fringes in two regions where $v \le v_1$ and $v \ge v_2$. In region I where $v \le v_1$, the first avoided crossing (M1) behaved as a beam splitter and the second as a total reflector. In region II where $v \ge v_2$, the first avoided crossing was completely transparent and the second functioned as a beam splitter, as indicated in Fig. 4.4 (d). For both regions, phase difference was accumulated along the two separate paths after passing the beam splitter. Assume the phase difference starts to accumulate at t=0. Then after the adiabatic evolution of period Δt, the phase difference is given by

$$\varphi(\Delta t) = \frac{1}{\hbar}\int_0^{\Delta t}\left[E_1(t) - E_2(t)\right]dt\ , \qquad (4.5)$$

where $E_1(t)$ and $E_2(t)$ are the instantaneous eigenenergies along the two paths, respectively. By considering both the phase jump in the LZ transitions and the total accumulated phase difference during the adiabatic evolutions, the constructive

interference fringes can be calculated analytically. The calculated fringes at region I and II are shown in Fig. 4.4 (b) and (c), which agree very well with the measured interference fringes. The detail of the analytical calculations is described in [73].

For the intermediate regions, one has to perform numerical simulations to calculate the occupation probability of $|1g_1g_2\rangle$. The time-dependent density operator ρ can be obtained by solving the Bloch density matrix equation

$$\dot{\rho} = -\frac{i}{\hbar}\left[\hat{H}, \rho\right] - \Gamma[\rho], \tag{4.6}$$

where $\Gamma[\rho]$ is related to the measured decoherence times [74]. By expanding the bipartite Hamiltonian in Eq. (4.1) to a tripartite system, we have

$$\hat{H} = \begin{pmatrix} \hbar\omega_{10} & -\Delta_1/2 & -\Delta_2/2 \\ -\Delta_1/2 & \hbar\omega_{TLS1} & 0 \\ -\Delta_2/2 & 0 & \hbar\omega_{TLS2} \end{pmatrix}. \tag{4.7}$$

The result of the numerical calculation agrees excellently with the measured LZS interference pattern, as shown in Fig. 4.5.

In this section, a new approach to precisely control multi-partite quantum states has been demonstrated by the realization of LZS interference in the coupled qubit-TLS system and the remarkable agreement between the theoretical and experiment results. With all the system parameters carefully calibrated, one can perform precise manipulation of quantum states via controlled LZ transitions. Furthermore, this method can be developed to realize various fast multi-qubit gates.

4.4 Creating the W state in a tripartite quantum system via LZ transitions

Interestingly, we can manipulate the state of a tripartite system to create entangled states such as W state through coherent LZ transitions. The general form of

the wavefunction of the tripartite quantum system we studied can be written as

$$|\psi\rangle = \alpha|1g_1g_2\rangle + \beta|0e_1g_2\rangle + \gamma|0g_1e_2\rangle, \tag{4.8}$$

where α, β, and γ are complex numbers.

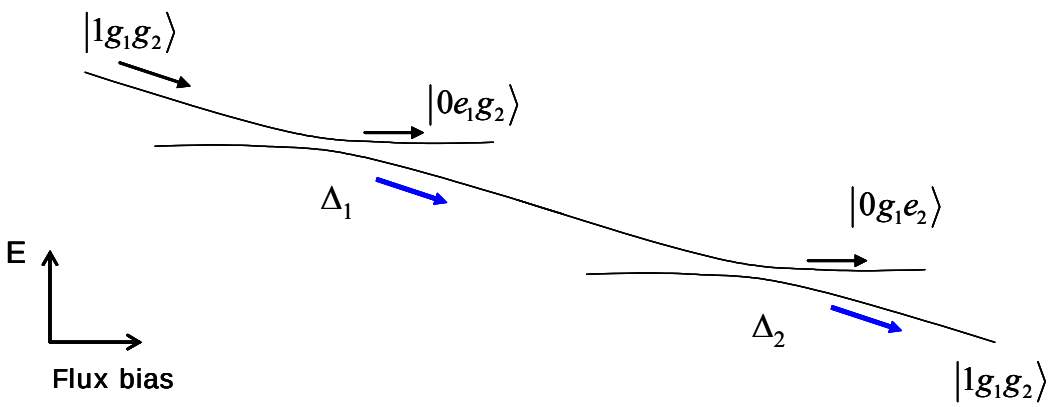

Fig. 4.6. Schematic drawing of sweeping flux bias through two avoided level crossings with respective tunnel splittings Δ_1 and Δ_2 in a tripartite system.

Suppose we prepare the system in $|1g_1g_2\rangle$ and then sweep the flux bias through two avoided level crossings with different sweeping rates, as shown in the Fig. 4.6. Denote the LZ transition probabilities at the two avoided crossings as P_{LZ1} and P_{LZ2}, respectively. Based on the state transformation due to one LZ transition as described by Eq. (4.3), the final state of the tripartite system after two successive LZ transitions is given by

$$|\psi\rangle = \sqrt{P_{LZ1}P_{LZ2}}\,|1g_1g_2\rangle + e^{-i\varphi_1}\sqrt{1-P_{LZ1}}\,|0e_1g_2\rangle + e^{-i\varphi_2}\sqrt{P_{LZ1}(1-P_{LZ2})}\,|0g_1e_2\rangle, \tag{4.9}$$

where φ_1 and φ_2 are the relative phase difference generated by the LZ transitions and adiabatic evolutions. It is straightforward to show that when $P_{LZ1} = \frac{2}{3}$ and $P_{LZ2} = \frac{1}{2}$, the final state

$$|\psi\rangle = \frac{1}{\sqrt{3}}\left(|1g_1g_2\rangle + e^{-i\varphi_1}|0e_1g_2\rangle + e^{-i\varphi_2}|0g_1e_2\rangle\right), \tag{4.10}$$

which is essentially a generalized W state. It won't be difficult to adjust the sweeping rates to set $P_{LZ1} = \frac{2}{3}$ and $P_{LZ2} = \frac{1}{2}$ if the magnitudes of the splittings have been accurately calibrated. Therefore, this approach only requires two consecutive linear sweepings of the flux bias with different sweeping rates to create the W state. In contrast, the conventional method of preparing the W state involves the use of a sequence of microwave pulses, which consist of two single-qubit gates and three two-qubit gates (CNOT). Thus using LZ transitions to manipulate tripartite quantum states is a much simpler approach in this case.

Furthermore, it is interesting to consider the gate speed using LZ transitions. Notice that in region II of the measured LZS interference pattern in Fig. 4.4 (a), constructive interference fringes occurred even when the duration of the triangle pulse was less than 10 ns. Thus the duration of the two consecutive sweepings of the flux bias required to generate the W state can be shorter than 5 ns. On the other hand, the time needed for each single-qubit gate and two-qubit gate using microwave pulses are typically on the order of 5 ns and 10 ns, respectively [75]. Therefore, the time needed to realize a W state using LZ transitions is much shorter than that required by the conventional method. It reveals that the coherent manipulation of the multipartite quantum states via LZ transitions is a very promising approach for a new family of fast multi-qubit quantum gates.

Chapter 5. Conclusions

Compared to other approaches to quantum computing, superconducting phase qubits based on rf SQUIDs are larger in size and thus allow stronger and more flexible inter-qubit coupling required by scalable quantum computing. On the other hand, phase qubits also strongly interact with the defects in the materials used to fabricate the qubit circuits and spurious environmental electromagnetic modes, resulting in significant decoherence. The measured energy relaxation time in our Al phase qubit was up to 73 ns. The dielectric loss has been considered as the dominant energy loss mechanism in superconducting phase qubits and the energy loss could be due to the dissipation from the TLS defects in amorphous dielectrics [33, 68]. Hence, in order to obtain longer T_1, the dielectric loss in the qubit circuits has to be reduced. Furthermore, phase qubits are also subject to pure dephasing induced by low frequency magnetic flux noise. From the Ramsey fringe experiment, we have accurately determined the pure dephasing time $T_\varphi = 81 \pm 2$ ns, corresponding to the rms of flux noise of 84 $\mu\Phi_0$. The pure dephasing time $T_{\varphi E} = 500 \pm 100$ ns was extracted from the spin echo signal. In addition, the spin echo signal was also well fitted to exponential decay, yielding decoherence time T_{2E} very close to $2T_1$. We also found there was no significant improvement in decoherence time when using the optimized second order dynamical decoupling pulse sequence. The result indicated that dephasing due to the low frequency flux noise was largely suppressed by the use of spin echo pulse and there was no significant effect of high frequency (>10 MHz) flux noise in the phase qubit.

One solution to the short coherence time problem in phase qubits is to develop faster multi-qubit gates. For this purpose, we investigated how to utilize the LZ transitions to control the multi-partite quantum states in a coupled qubit-TLS system. With the coherence times and all the parameters of the phase qubit carefully calibrated, we successfully demonstrated precise coherent manipulation of tripartite quantum states in a phase qubit coupled to two TLSs. The state manipulation was achieved by applying high-resolution triangle pulse into the readout pulse line to sweep the flux bias through two avoided level crossings, where the LZ transitions occurred with significant probability. The amplitude and duration of the triangle pulse were varied to measure the LZS interference patterns. The results of theoretical calculations based on the calibrated coherence times and qubit parameters agreed very well with the experimental results, indicating that the coherent control was precise and the calibrations were accurate. Finally we showed how to realize the W state in a tripartite quantum system by manipulating the quantum state via two successive LZ transitions. Compared to the conventional method using microwave pulses, this new method allows much simpler operation and much shorter gate time. Hence, coherent manipulation of multipartite quantum states via LZ transitions has great potential to be the foundation for a new family of fast multi-qubit gates for scalable quantum computing.

Bibliography

1. R. P. Feynman, *Simulating physics with computers. International Journal of Theoretical Physics* **21**, 467 (1982).
2. D. Deutsch, *Quantum-theory, the church-turing principle and the universal quantum computer. Proceedings of the Royal Society of London A* **400**, 97 (1985).
3. P. W. Shor, *Algorithms for quantum computation: discrete logarithms and factoring. Proc. 35th Annual Symposium on Foundations of Computer Science* 124-134 (1994).
4. Lov K. Grover, *Quantum mechanics helps in searching for a needle in a haystack. Phys. Rev. Lett.* **79**, 325-328 (1997).
5. M. A. Nielsen and I.L. Chuang, *Quantum Computation and Quantum Information*. 2000: Cambridge Press.
6. D. P. DiVincenzo, *The physical implementation of quantum computation. Fortschritte der Physik* **48**, 9 (2000).
7. E. Knill, R. Laflamme, and G.J. Milburn, *A scheme for efficient quantum computation with linear optics. Nature* **409**, 46 (2001).
8. J. L. O'Brien, *Optical quantum computing. Science* **318**, 1567 (2007).
9. A. Politi *et al*., *Silica-on-silicon waveguide quantum circuits. Science* **320**, 646 (2008).
10. J. I. Cirac and P. Zoller, *Quantum computations with cold trapped ions. Phys. Rev. Lett.* **74**, 4091 (1995).
11. D. Leibfried *et al*., *Creation of a six-atom 'Schrodinger cat' state. Nature* **438**, 639 (2005).
12. D. Stick *et al*., *Ion trap in a semiconductor chip. Nature Physics* **2**, 36 (2006).
13. J. P. Home, D. Hanneke, J.D.J.J.M. Amini, D. leibfried, and D.J. Wineland, *Complete methods set for scalable ion trap quantum information processing. Science* **325**, 1227 (2009).
14. A. J. Leggett and A. Garg, *Quantum mechanics versus macroscopic realism: is the flux there when nobody looks? Phys. Rev. Lett.* **54**, 857 (1985).
15. A. O. Caldeira and A.J. Leggett, *Quantum tunneling in a dissipative system. Ann. Phys. (NY)* **149**, 347 (1983).
16. A. Wallraff *et al.*, *Strong coupling of a single photon to a superconducting qubit using circuit quantum electrodynamics. Nature* **431**, 162 (2004).
17. L. DiCarlo *et al.*, *Demonstration of two-qubit algorithms with a superconducting quantum processor. Nature* **460**, 240 (2009).
18. B. D. Josephson, *Possible new effects in superconductive tunnelling. Physics Letters* **1**, 251 (1962).
19. R. F. Voss and R.A. Webb, *Macroscopic quantum tunneling in 1-μm Nb Josephson junctions. Phys. Rev. Lett.* **47**, 265 (1981).
20. M. H. Devoret, J.M. Martinis, and J. Clarke, *Energy-level quantization in the zero-voltage state of a current-biased Josephson junction. Phys. Rev. Lett.* **55**, 1543 (1985).
21. D. E. McCumber, *Tunneling and weak-link superconductor phenomena having*

potential device applications. J. Appl. Phys. **39**, 2503 (1968).
22. R. Rouse, S. Han, and J.E. Lukens, *Observation of resonant tunneling between macroscopically distinct quantum levels. Phys. Rev. Lett.* **75**, 1614 (1995).
23. R. Rouse, S. Han, and J.E. Lukens, *Quantum coherence and decoherence*. 1996. 179.
24. S. Han, R. Rouse, and J.E. Lukens, *Generation of a population inversion between quantum states of a macroscopic variable. Phys. Rev. Lett.* **76**, 3404 (1996).
25. S. Han, R. Rouse, and J.E. Lukens, *Observation of cascaded two-photon-induced transitions between fluxoid states of a SQUID. Phys. Rev. Lett.* **84**, 1300 (2000).
26. J. R. Friedman, V. Patel, W. Chen, S.K. Tolpygo, and J.E. Lukens, *Quantum superposition of distinct macroscopic states. Nature* **406**, 43 (2000).
27. C. H. van der Wal *et al.*, *Quantum superposition of macroscopic persistent-current states. Science* **290**, 773 (2000).
28. Y. Nakamura *et al*., *coherent control of macroscopic quantum states in a single Cooper-pair box. Nature* **398**, 786 (1999).
29. Y. Yu *et al.*, *Coherent temporal oscillations of macroscopic quantum states in a Josephson junction. Science* **296**, 889 (2002).
30. J. M. Martinis *et al*., *Rabi oscillations in a large Josephson-junction qubit. Phys. Rev. Lett.* **89**, 117901 (2002).
31. I. Chiorescu, Y. Nakamura, C.M. Harmans, and J.E. Mooij, *Coherent quantum dynamics of a superconducting flux qubit. Science* **299**, 1869 (2003).
32. K. B. Cooper *et al.*, *Observation of quantum oscillations between a Josephson phase qubit and a microscopic resonator using fast readout. Phys. Rev. Lett.* **93**, 180401 (2004).
33. J. M. Martinis *et al*., *Decoherence in Josephson qubits from dielectric loss. Phys. Rev. Lett.* **95**, 210503 (2005).
34. M. Steffen *et al.*, *State tomography of capacitively shunted phase qubits with high fidelity. Phys. Rev. Lett.* **97**, 050502 (2006).
35. M. Steffen *et al.*, *Measurement of the entanglement of two superconducting qubits via state tomography. Science* **313**, 1423 (2006).
36. M. Ansmann *et al.*, *Violation of Bell's inequality in Josephson phase qubits. Nature* **461**, 504 (2009).
37. S. Han, J. Lapointe, and J.E. Lukens, *Effect of a two-dimensional potential on the rate of thermally induced escape over the potential barrier. Phys. Rev. B* **46**, 6338 (1992).
38. Wangsness, R.K. and F. Bloch, *The dynamical theory of nuclear induction. Phys. Rev.* **89**, 728 (1953).
39. J. M. Martinis *et al*., *Experimental tests for the quantum behavior of a macroscopic degree of freedom: the phase difference across a Josephson junction. Phys. Rev. B* **35**, 4682 (1987).
40. M. H. Devoret, *Quantum Fluctuations*, ed. S. Reynaud *et al*. 1995.
41. P. Ullersma, *Physica (Utrecht)* **32**, 27 (1966).
42. A. O. Caldeira and A.J. Leggett, *Influence of dissipation on quantum tunneling in macroscopic systems. Phys. Rev. Lett.* **46**, 211 (1981).

43. U. Weiss, *quantum dissipative systems*. 1999.
44. A. J. Leggett *et al*., *Dynamics of the dissipative two-state system. Rev. Mod. Phys.* **59**, 1 (1987).
45. B. Mao and S. Han, *Measurement of environmental impedance at plasma frequency of Josephson junction with microwave enhanced thermal escape. IEEE Trans. Appl. Supercond.* **17**, 94 (2007).
46. F. C. Wellstood *et al*., *Low-frequency noise in dc superconducting quantum interference devices below 1 K. Appl. Phys. Lett.* **50**, 772 (1987).
47. F. Yoshihara *et al*., *Decoherence of flux qubits due to 1/f flux noise. Phys. Rev. Lett.* **97**, 167001 (2006).
48. T. Lanting *et al*., *Geometrical dependence of the low-frequency noise in superconducting flux qubits. Phys. Rev. B* **79**, 060509 (2009).
49. R. C. Bialczak *et al.*, *1/f flux noise in Josephson phase qubits. Phys. Rev. Lett.* **99**, 187006 (2007).
50. R. H. Koch, D.P. DiVincenzo, and J. Clark, *Model of 1/f flux noise in SQUIDs and qubits. Phys. Rev. Lett.* **98**, 267003 (2007).
51. Sousa, R., *Dangling-bond spin relaxation and magnetic 1/f noise from amorphous-semiconductor/oxide interface. Phys. Rev. B* **76**, 245306 (2007).
52. L. Faoro and L.B. Ioffe, *Microscopic origin of low-frequency flux noise in Josephson circuits. Phys. Rev. Lett.* **100**, 227005 (2008).
53. H. Bluhm *et al*., *Spinlike susceptibility of metallic and insulating thin films at low temperature. Phys. Rev. Lett.* **103**, 026805 (2009).
54. K. M. Lang, S. Nam, J. Aumentado, C. Urbina, and J.M. Martinis, *Banishing quasiparticles from Josephson-junction qubits: why and how to do it. IEEE Trans. Appl. Supercond.* **13**, 989 (2003).
55. W. Chen, V. Patel, and J.E. Lukens, *Fabrication of high-quality Josephson junctions for quantum computation using a self-aligned process. Microelectronic Engineering* **73-74**, 767 (2004).
56. B. Mao, W. Qiu, and S. Han, *Temperature dependence of magnetism in dc SQUIDs and rf SQUID flux qubit in nT fields. Supercond. Sci. Technol.* **23**, 045027 (2010).
57. E. Lucero *et al*, *High fidelity gates in a single Josephson qubit. Phys. Rev. Lett.* **100**, 247001 (2008).
58. M. H. S. Amin and D.V. Averin, *Macroscopic resonant tunneling in the presence of low frequency noise. Phys. Rev. Lett.* **100**, 197001 (2008).
59. W. Qiu, Y. Yu, B. Mao, S. Li, and S. Han, *Temperature dependence of the energy relaxation rate in an RF-SQUID flux qubit. IEEE Trans. Appl. Supercond.* **19**, 977 (2009).
60. D. Bennett, L. Longobardi, V. Patel, W. Chen, and J.E. Lukens, *Rf-SQUID qubit readout using a fast flux pulse. Supercond. Sci. Technol.* **20**, S445 (2007).
61. R. Harris *et al*., *Probing noise in flux qubits via macroscopic resonant tunneling. Phys. Rev. Lett.* **101**, 117003 (2008).
62. C. Cohen-Tannoudji *et al*., *Quantum mechanics*. 1977. p. 1322.
63. Because the number of the data points in the spectrum (Fig. 4.2) is too small, we couldn't extract the intrinsic line width by deconvolution. Instead, based on the

measured line width of the resonant peak and T_1, we obtained the intrinsic line width by numerically simulating the convolution.
64. G. Ithier *et al*, *Decoherence in a superconducting quantum bit circuit. Phys. Rev. B* **72**, 134519 (2005).
65. E. L. Hahn, *Spin echoes. Physical Review* **80**, 580 (1950).
66. G. S. Uhrig, *Keeping a quantum bit alive by optimized π-pulse sequences. Phys. Rev. Lett.* **98**, 100504 (2007).
67. J.F. Du *et al*, *Preserving electron spin coherence in solids by optimal dynamical decoupling. Nature* **461**, 1265 (2009).
68. R. O. Pohl, X. Liu, and E. Thompson, *Low-temperature thermal conductivity and acoustic attenuation in amorphous solids. Rev. Mod. Phys.* **74**, 991 (2002).
69. J. M. Martinis, *Superconducting phase qubits. Quantum Inf Process* **8**, 81 (2009).
70. M. Neeley *et al*., *Process tomography of quantum memory in a Josephson-phase qubit coupled to a two-level state. Nature Physics* **4**, 523 (2008).
71. J. Johansson et al., *Vacuum Rabi oscillations in a macroscopic superconducting qubit LC oscillator system. Phys. Rev. Lett.* **96**, 127006 (2006).
72. S. N. Shevchenko, S. Ashhab, and F. Nori, *Landau-Zener-Stuckelberg interferometry. Physics Reports* **492**, 1 (2010).
73. G.Z. Sun, W.X. Da, B. Mao, J. Chen, Y. Yu, P.H. Wu, and S. Han, *Tunable mirrors for quantum manipulation of a hybrid tripartite qubit system. submitted to Nature communications* (2010).
74. Z.Y. Zhou, S. Chu, and S. Han, *Relaxation and decoherence in a resonantly driven qubit. J. Phys. B: At. Mol. Opt. Phys.* **41**, 045506 (2008).
75. M. Neeley *et al*., *Generation of three-qubit entangled states using superconducting phase qubits.* arXiv:1004.4246 (2010).

Appendix

A. Hamiltonian of an rf SQUID phase qubit under microwave radiation

Consider an rf SQUID interacting with microwave and denote $\Phi_{rf}\sin\omega t$ as the induced rf magnetic flux in the SQUID loop. Thus the Hamiltonian of the rf SQUID can be written as $H = H_0 + H_I$, where the unperturbed Hamiltonian H_0 is given by Eqs. (1.7) and (1.12), and the interaction term $H_I = -\frac{\Phi_{rf}}{L}\sin\omega t\hat{\Phi}$. By choosing the ground state and excited state localized in the higher potential well as the qubit's computational basis states $|0\rangle$ and $|1\rangle$ respectively, one has $\hat{H}_0|0\rangle = E_0|0\rangle$ and $\hat{H}_0|1\rangle = E_1|1\rangle$. Thus $\hat{H}_0 = -\frac{\hbar\omega_{10}}{2}\sigma_z$, where $\hbar\omega_{10} = E_1 - E_0$ is the energy difference between the qubit states. To find out the matrix elements of operator $\hat{\Phi}$, notice that around the bottom of a deep well where the potential barrier is much greater than $\hbar\omega_{10}$, the potential is approximately harmonic. Hence, the diagonal matrix elements of $\hat{\Phi}$ are equal $\langle 0|\hat{\Phi}|0\rangle = \langle 1|\hat{\Phi}|1\rangle$, and they only produce an identity matrix, which doesn't change the qubit state and thus is negligible. In the approximation of harmonic potential, using the fact that the effective mass of the system is capacitance *C*, one has $\hat{\Phi} = c_1\sigma_x$, where $c_1 = \langle 0|\hat{\Phi}|1\rangle = \langle 1|\hat{\Phi}|0\rangle = \sqrt{\frac{\hbar}{2C\omega_{10}}}$. Consequently, the interaction Hamiltonian could be written as

$$H_I = -c_1 I_{rf}\frac{e^{i\omega t} - e^{-i\omega t}}{2i}\sigma_x, \qquad \text{(A.1)}$$

where $I_{rf} \equiv \Phi_{rf}/L$. In the interaction picture, the interaction Hamiltonian is transformed into $\bar{H}_I = U^\dagger H_I U$, where $U = \exp(-i\hat{H}_0 t/\hbar) = \exp(i\omega_{10}t\sigma_z/2)$. Thus

$$\bar{H}_I = -\frac{c_1 I_{rf}}{2i}\left(e^{i\omega t} - e^{-i\omega t}\right)\begin{pmatrix} 0 & e^{-i\omega_{10}t} \\ e^{i\omega_{10}t} & 0 \end{pmatrix}$$

$$= -\frac{c_1 I_{rf}}{2i}\begin{pmatrix} 0 & e^{i(\omega-\omega_{10})t} - e^{-i(\omega+\omega_{10})t} \\ e^{i(\omega_{10}+\omega)t} - e^{-i(\omega-\omega_{10})t} & 0 \end{pmatrix}. \quad \text{(A.2)}$$

Assume the detuning $\Delta\omega = \omega - \omega_{10} << \omega + \omega_{10}$. The fast oscillating terms will be averaged out and thus their effects on qubit dynamics are negligible. Such an approach is called the rotating wave approximation (RWA). After RWA and back to the Schrödinger picture, one has

$$H_I = -\frac{c_1 I_{rf}}{2i}\begin{pmatrix} 0 & e^{i\omega t} \\ -e^{-i\omega t} & 0 \end{pmatrix}. \quad \text{(A.3)}$$

The interaction Hamiltonian in Eq. (A.3) is still time-dependent. In order to eliminate the time-dependent terms, consider the Hamiltonian in the frame rotating about the *z*-axis with the angular frequency equal to ω. In such a rotating frame, the new qubit state vector is then given by $|\psi'\rangle = R_z(\omega t)|\psi\rangle$, where $R_z(\omega t)$ is a rotation operator about the *z*-axis by an angle of ωt. Consequently, the total Hamiltonian of the rf SQUID phase qubit becomes time-independent

$$H_{qubit} = -\hbar\left(\Delta\omega\frac{\sigma_z}{2} + \Omega_0\frac{\sigma_y}{2}\right) \quad \text{(A.4)}$$

where $\Omega_0 = \langle 0|\hat{\Phi}|1\rangle I_{rf}/\hbar = \sqrt{\frac{1}{2C\hbar\omega_{10}}}I_{rf}$ is the angular frequency of on-resonance Rabi oscillation.

B. Cryogenic low pass filters

B.1 Low pass LC filters

The design of a 3-pole "T" type low pass LC filter with cutoff frequency ~ 2 MHz is shown in Fig B.1. The filter was made with ATC wire-wound chip inductors and Novacap chip capacitors. The transmission property of the engineered low pass LC filter was measured using a network analyzer, as illustrated in Fig B.2. The LC filter works well at frequencies lower than 250 MHz. However at higher frequencies, the performance became worse due to the parasitic shunting capacitance and serial inductance in the circuit at high frequency. Hence, it is necessary to use copper powder filter to attenuate the high frequency noise.

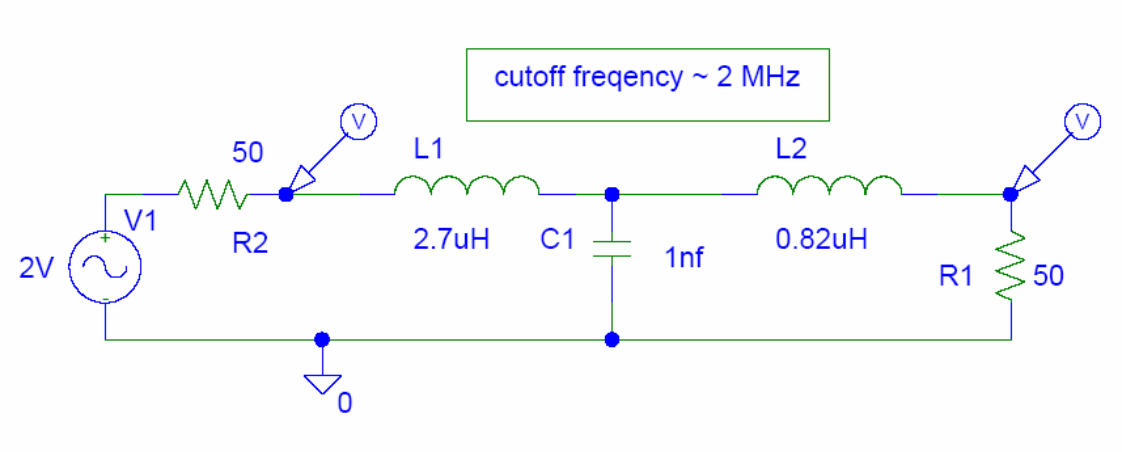

Fig B.1. Design of a circuit including a 3-pole low pass LC filter, which consists of two inductances L_1= 2.7 μH and L_2= 0.82 μH and one capacitor C_1= 1 nF. The simulation showed that the cutoff frequency of the LC filter is about 2 MHz.

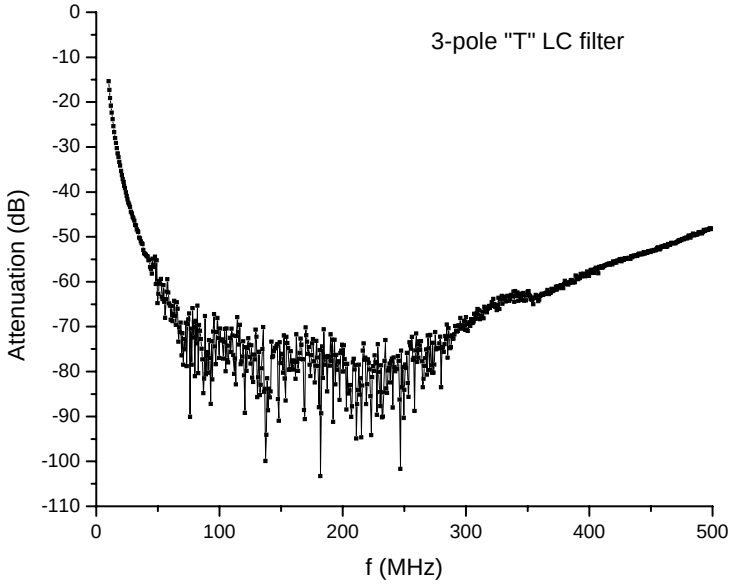

Fig. B.2. Measured transmission property of the 3-pole LC filter which has the configuration as shown in Fig. B.1.

B.2 Integrated LC-copper powder filters (CPFs)

The housing of CPF was made of oxygen-free copper tube (OD=6.35 mm, ID≈4.7 mm). A 1.5 m long and 0.254 mm thick tinned copper wire was wound to form a 9 cm long coil with the outer diameter equal to 2.5 mm. The LC filter was integrated in the middle of the coil. The coil was then placed inside the tube and insulated from the tube by a thin paper tube. Subsequently, the copper powder (Alfa Aesar, 3-5 micron) was filled in the tube and hardened by the injected Epoxy (Bipax BA-2115). The ends of the filter were sealed with two SMA connectors by soldering.

As shown in Fig B.3 and B.4, the engineered integrated LC CPF performs very well. More than 90 dB attenuation, limited by the instrument's noise floor, was obtained at frequencies higher than 400 MHz. In addition, the measured cutoff frequency of the integrated LC-CPF was about 5 MHz.

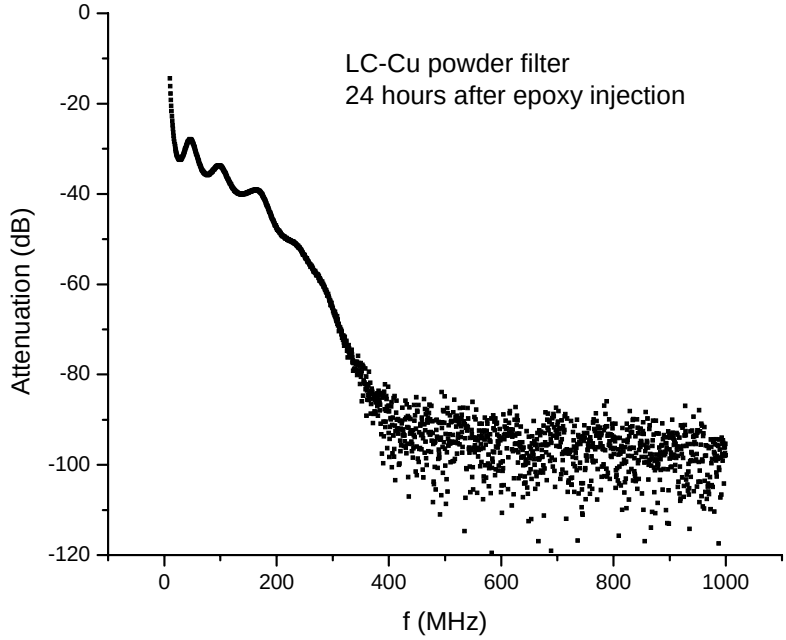

Fig. B.3. Transmission property of LC-CPF measured at frequencies up to 1 GHz at room temperature.

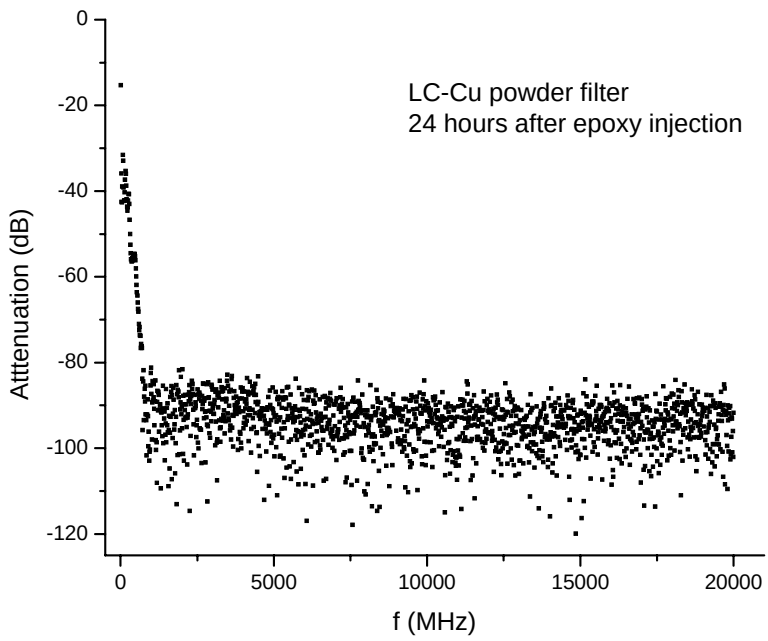

Fig. B.4. Transmission property of LC-CPF measured at frequencies up to 20 GHz at room temperature.

B.3 Low pass RC filters

The LC-CPF was thermally anchored onto the mixing chamber of the dilution fridge, while the low pass RC filters were mounted on the 1 K pot where T ~ 1.4 K. The designs of the RC filters for flux bias and dc SQUID readout lines are shown in Fig. B.5.

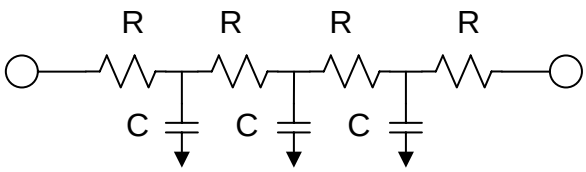

Fig. B.5. Schematic of low pass RC filters. For those in the flux bias lines, R= 249 Ω, C= 680 pF, while for those in the dc SQUID lines, R= 2.49 kΩ, C= 68 pF.

The cutoff frequency for both designs is a few hundred kHz. The resistance of the four metal film resistors in the flux bias lines was smaller than that in the dc SQUID current bias and voltage sensing lines because the flux bias lines typically carry much larger current (~ 1 mA) than the dc SQUID lines (~ 1 μA). Note that the cooling power of 1 K pot is on the order of 10^2 mW. The Joule heating on the resistors could be a problem if the resistance is too large.

C. L/C dependence of MRT-peak spacing around $\Phi_x = \Phi_0/2$

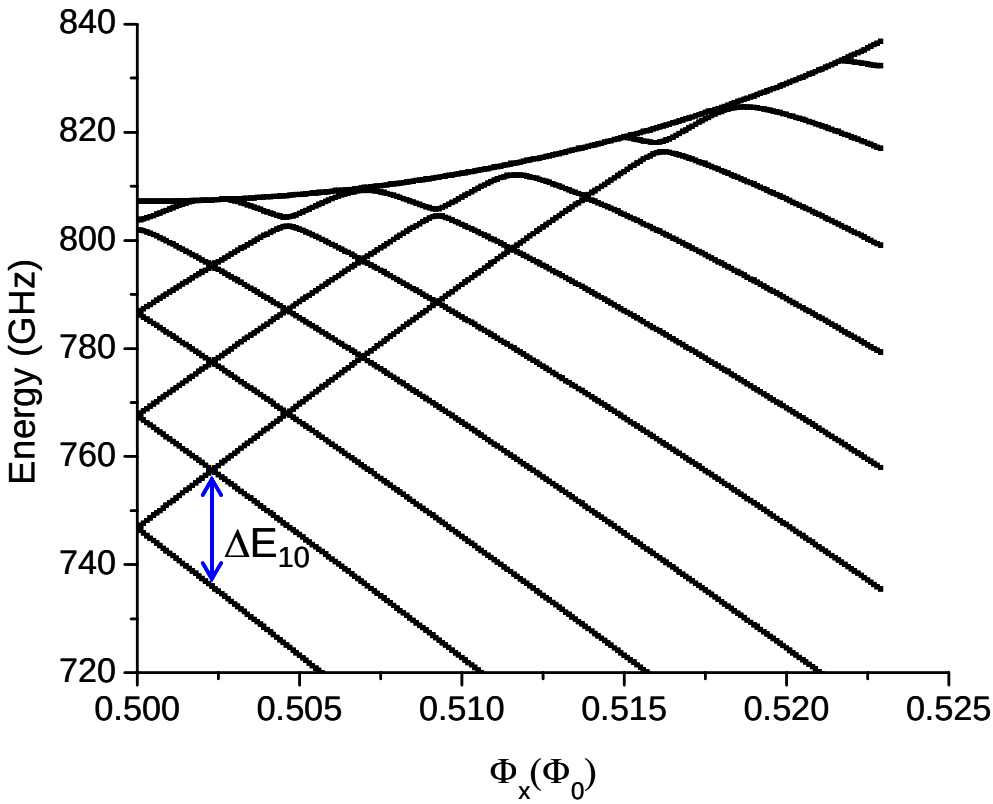

Fig. C.1. Energy level diagram of the Nb sample LLC6 where $\beta_L = 1.31$, $L = 267$ pH, and C=110 fF. The energy levels shown here are those below the top of the barrier (the top curve).

Before deriving the equation relating the spacing between two adjacent MRT peaks to the value of L/C, let's look at a typical energy level diagram of an rf SQUID, as shown in Fig. C.1. The energies of eigenstates were calculated as a function of external flux bias by solving the stationary Schrödinger equation. The top curve indicates the top of the potential barrier and in the figure we only show the energy levels below the barrier top. The curves with positive slopes correspond to the energy levels in the left well, while those with negative slopes are in the right well. Actually,

the slope represents the circulating current in SQUID loop, *i.e.*, $I_p = -\frac{\partial E}{\partial \Phi_x}$. When the external flux bias is increased from $\Phi_0/2$, the potential is tilted so that the left well becomes higher and shallower. Meanwhile, the energy level of the ground state in the left well, *i.e.*, the lowest curve with positive slope, will be aligned with the energy levels in the right well. In this process, MRT occurs at each avoided level crossing.

As indicated by the blue arrows in Fig. C.1, at the flux bias where the first avoided crossing occurs, the energy difference between the lowest two levels in the right well ΔE_{10} is equal to that between the ground states in opposite wells. Thus ΔE_{10} is related to I_p by $\Delta E_{10} = 2I_p \Delta\Phi_{x\_MRT}$, where $\Delta\Phi_{x\_MRT}$ denotes the location of the first avoided crossing with respect to $\Phi_0/2$ and is equal to the MRT peak spacing around $\Phi_x = \Phi_0/2$. On the other hand, in a deep well where the potential barrier height $\Delta U >> \hbar\omega_{10}$, ΔE_{10} can be approximated by $\hbar\omega_p$, where ω_p is the small oscillation frequency at the bottom of the well. According to Eq. (3.2), $\omega_p = \sqrt{\frac{1+\beta_L \cos(2\pi\phi_b)}{LC}}$ where ϕ_b is the location of the left well's bottom normalized to Φ_0. By defining $\frac{\varphi_m}{2\pi}\Phi_0 = LI_p$, one can show that $\beta_L = \varphi_m / \sin\varphi_m$ and $\phi_b = 0.5 - \frac{\varphi_m}{2\pi}$. Consequently, we have

$$\Delta\Phi_{x\_MRT} = \frac{h}{2\Phi_0}\sqrt{L/C}\sqrt{1-\varphi_m/\tan\varphi_m}/\varphi_m . \qquad \text{(C.1)}$$